ETH Zürich
Master of Science ETH in Physics

Search for decays of the 125 GeV Higgs boson into a photon and a ϕ, ω or D^{*0} meson

MASTER THESIS

Author:
Martí Pedemonte Bernat

Supervisors:
Prof. Dr. Günther Dissertori, ETH Zürich
Prof. Dr. Christoph M. E. Paus, MIT
Dr. Mariarosaria D'Alfonso, MIT

Conducted at:
Particle Physics Collaboration, Massachusetts Institute of Technology

Cambridge MA, November 2023

Eidgenössische Technische Hochschule Zürich
Swiss Federal Institute of Technology Zurich

Massachusetts Institute of Technology

Acknowledgements

First acknowledgement.

Second acknowledgement.

Third acknowledgement.

Abstract

English abstract.

Catalan abstract

Put some keywords.

Contents

Introduction

This is the introduction.

Chapter 1

Theory and Motivation

This chapter aims to provide an overview of the Standard Model of Particle Physics (SM), with a specific focus on the important role played by the Higgs boson. We will give a brief introduction to the SM and its fundamental particles, discuss the Lagrangian that governs their behaviour, and explore their interactions represented by Feynman diagrams. Moreover, we will examine the characteristics of the Higgs boson — its properties, its most frequent production and decay modes, and the Yukawa couplings to the three different fermion families. Finally, we will concentrate on the decay channels subject of our analysis, and explore how a significant discrepancy between the measurements of these decay modes and the SM predictions might lead to new physics beyond the SM.

1.1 The Standard Model

One of the traits that distinguishes humans from other life forms is our sense of curiosity. Since ancient times, we have been trying to explain what happens around us, enabling us to predict and potentially harness the laws of nature. An exceptional theory that has come very close to achieving this goal is the Standard Model of Particle Physics (SM). It stands as one of the most precise theories ever conceived by humanity, and is the most successful theory of particle physics to date. The Standard Model serves as a theory capable of describing three of the four known fundamental forces in the Universe (electromagnetic, weak and strong forces, but not gravity). This is achieved by classifying a set of elementary particles and defining the interactions between them. Summaries of the SM can be found in Refs. [1, 2] among many others.

More in detail, the SM is a quantum field theory (QFT) defined by an internal local $SU(3)_C \times SU(2)_L \times U(1)_Y$ gauge symmetry. Each elementary particle has its corresponding field in the theory and is categorized as a fermion or a boson based on its spin (half-integer-spin particles are fermions, whereas integer-spin particles are bosons). There are twelve fermions organized into three families or generations of four members: a charged lepton (e.g., the electron), a neutral lepton (neutrino), an up-type quark and a down-type quark (in addition, each particle has its own corresponding antiparticle) (see Figure 1).

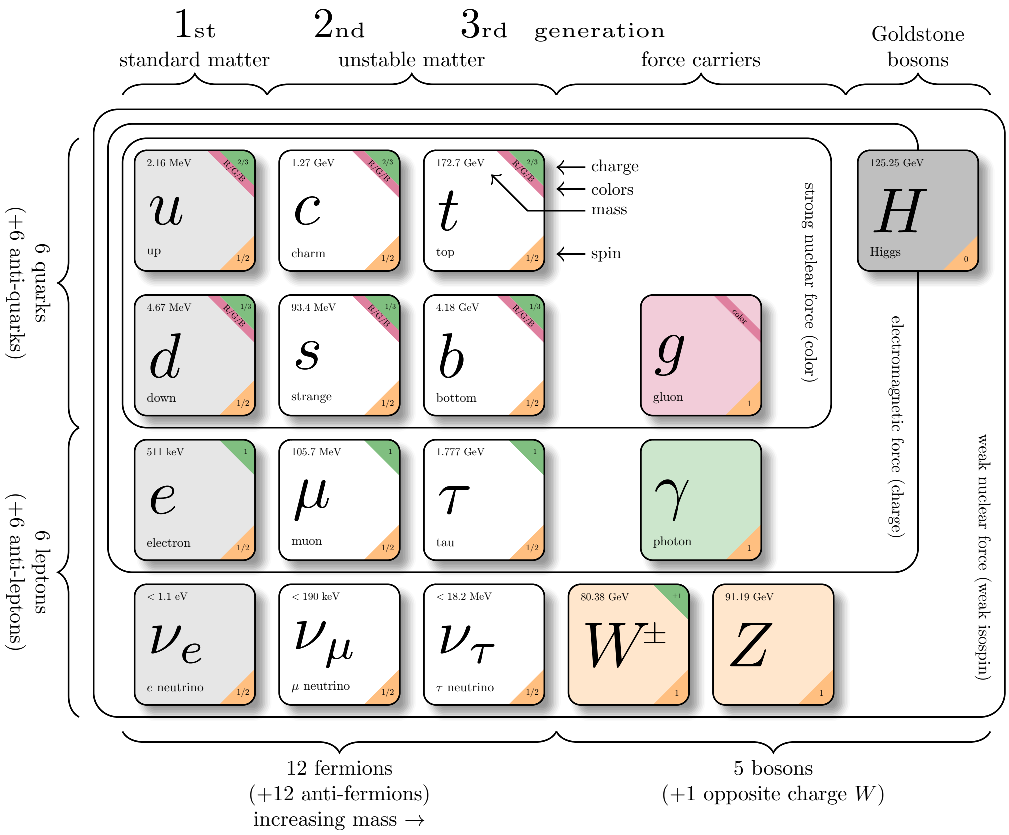

Figure 1: Elementary particles of the Standard Model. The electric charge, mass and spin of each particle are shown. Figure from Ref. [3].

These three factors of the gauge symmetry group give rise to the three fundamental interactions between fermions, which are mediated by gauge bosons. To be precise, each generator of a local invariant gauge group induces a massless gauge boson. In the same way that in quantum electrodynamics (QED), the local gauge invariance of the theory under the U(1) group leads to the existence of a massless gauge field A_μ (the photon field), in the SM, the process is analogous.

The invariance of the SM under $\mathrm{SU}(3)_\mathrm{C}$ postulates the existence of the gluon. More precisely, the eight generators of $\mathrm{SU}(3)_\mathrm{C}$ introduce eight gluons that mediate the strong force between particles that possess color charge (quarks and gluons). This is known as the quantum chromodynamics (QCD) sector of the Standard Model.

Similarly, the invariance of the second and third factors $\mathrm{SU}(2)_\mathrm{L} \times \mathrm{U}(1)_\mathrm{Y}$ indicates the existence of the photon, the Z^0 and the $W^\pm$ bosons. In this case, unlike in QED or QCD, we cannot directly associate the photon with the generator of the hypercharge group $\mathrm{U}(1)_\mathrm{Y}$ and the Z^0, $W^\pm$ bosons with the generators of the left weak isospin group $\mathrm{SU}(2)_\mathrm{L}$. Instead, the generators of $\mathrm{SU}(2)_\mathrm{L} \times \mathrm{U}(1)_\mathrm{Y}$ give rise to four intermediate vector bosons ($W_\mu^{1,2,3}$ for $\mathrm{SU}(2)_\mathrm{L}$ and B_μ for $\mathrm{U}(1)_\mathrm{Y}$), which are then mixed through the weak mixing angle or Weinberg angle,

θ_{W}, to produce the physical γ (A_μ), Z^0, $W^\pm$. The physical bosons are then defined as:

$$W_\mu^\pm = \frac{1}{\sqrt{2}}(W_\mu^1 \mp iW_\mu^2)$$
$$\begin{pmatrix} A_\mu \\ Z_\mu^0 \end{pmatrix} = \begin{pmatrix} \cos\theta_{\mathrm{W}} & \sin\theta_{\mathrm{W}} \\ -\sin\theta_{\mathrm{W}} & \cos\theta_{\mathrm{W}} \end{pmatrix} \begin{pmatrix} B_\mu \\ W_\mu^3 \end{pmatrix}$$

By the definition of the groups $\mathrm{SU}(2)_{\mathrm{L}}$ and $\mathrm{U}(1)_{\mathrm{Y}}$, the field $W_\mu^{1,2,3}$ couples only to left-handed (negative helicity) particles, whereas the hypercharge field B_μ couples to both left and right components with the same strength. Therefore, the intermediate boson mixing implies that $W^\pm$ only couple to left-handed particles, but Z^0 couples to both left and right-handed particles with different strengths, inducing (non-maximal) parity violation.

All gauge bosons that arise from the generators of gauge-invariant groups are expected to be massless; otherwise, the principle of local gauge invariance is spoiled and the theory becomes unrenormalizable. However, this contradicts experimental observations, which confirm that the Z^0 and $W^\pm$ bosons are, in fact, massive. This breaking of gauge invariance when giving a mass to a particle is not restricted only to gauge bosons but also happens for fermions. In the SM, to allow for massive fields, all particles obtain their masses using spontaneous symmetry breaking (SSB) via the Higgs mechanism.

Spontaneous symmetry breaking is a fundamental principle of QFT used to explain how gauge bosons (and, in general, massive particles) can acquire non-vanishing mass while maintaining the theory gauge-invariant. This process describes systems where the Lagrangian obeys symmetries, but the lowest-energy vacuum solutions do not exhibit the same symmetries. In the case of the Higgs mechanism, it relies on the existence of an $\mathrm{SU}(2)$ doublet complex scalar field ϕ with hypercharge $Y = +1$, which can be written as

$$\phi = \begin{pmatrix} \phi^+ \\ \phi^0 \end{pmatrix}$$

with $(\phi^+)^* = \phi^-$ and $(\phi^0)^* = \phi^0$. This scalar field has a Lagrangian density given by $\mathcal{L} = |D_\mu\phi|^2 - V(\phi)$ and a potential $V(\phi) = \mu^2\phi^\dagger\phi + \lambda(\phi^\dagger\phi)^2$, where D_μ is the covariant derivative determined by $\mathrm{SU}(2)_{\mathrm{L}} \times \mathrm{U}(1)_{\mathrm{Y}}$. When expanding the field ϕ around a minimum of the potential V, one finds out that there are infinitely many values of ϕ that minimize the potential. Suppose one expands ϕ around

$$\phi_0 = \frac{1}{\sqrt{2}}\begin{pmatrix} 0 \\ v \end{pmatrix}, \quad \text{so} \quad \phi(x) = \frac{1}{\sqrt{2}}\begin{pmatrix} 0 \\ v + h(x) \end{pmatrix}.$$

Deciding to expand the field around a chosen minimum ϕ_0 spontaneously breaks the $\mathrm{SU}(2)_{\mathrm{L}} \times \mathrm{U}(1)_{\mathrm{Y}}$ symmetry, which in turn generates mass terms for the weak bosons in the Lagrangian. To convince oneself of the last implication it suffices to expand the $|D_\mu\phi|^2$ term around the chosen vacuum expectation value v, which will produce terms of the form $M_W^2 W_\mu^+ W^{-\mu}$ and $M_Z^2 Z_\mu^0 Z^{0\mu}$ in the Lagrangian density. This scalar field is called the Higgs field.

With that, the Standard Model of particle physics is governed by the following Lagrangian density:

$$\begin{aligned} \mathcal{L}_{\text{SM}} = &-\frac{1}{4}G^a_{\mu\nu}G^{a\mu\nu} - \frac{1}{4}W^i_{\mu\nu}W^{i\mu\nu} - \frac{1}{4}B_{\mu\nu}B^{\mu\nu} \\ &+ \left|D_\mu\phi\right|^2 - \mu^2\phi^\dagger\phi - \lambda(\phi^\dagger\phi)^2 \\ &+ i\left[\bar{L}\not{D}L + \bar{e}\not{D}e + \bar{Q}\not{D}Q + \bar{u}\not{D}u + \bar{d}\not{D}d\right] \\ &- \left[Y_e\bar{L}\phi e + Y_u\bar{Q}\phi^c u + Y_d\bar{Q}\phi d + \text{h.c.}\right] \end{aligned} \tag{1}$$

The used notation is the following: ϕ, Q, u, d, L, e are the SM Higgs, quarks and lepton fields. The left-handed doublets are denoted by capital letters as

$$Q_i = \begin{pmatrix} u^i_L \\ d^i_L \end{pmatrix} \text{ for quarks, and } L_\alpha = \begin{pmatrix} \nu^\alpha_L \\ e^\alpha_L \end{pmatrix} \text{ for leptons,}$$

whereas for the right-handed singlets lowercase letters are used. We use the usual covariant derivative defined as

$$D_\mu = \partial_\mu - ig_s T^a G^a_\mu - ig\frac{\sigma^i}{2}W^i_\mu - ig'\frac{Y}{2}B_\mu$$

and where T^a, σ^i (Pauli matrices) and Y (weak hypercharge) are the generators of SU(3), SU(2) and SU(1) respectively, and g_s, g and g' are the coupling constants. ϕ^c is the charge conjugate of ϕ defined by $\phi^c = i\frac{\sigma_2}{2}\phi^\dagger$.

The first line in Equation (1) describes the kinetic energies and interactions of the gauge boson fields. The field strength tensors associated to G^a_μ (gluons), W^i_μ and B_μ ($W^\pm$, Z^0, γ) are defined by

$$\begin{aligned} G^a_{\mu\nu} &= \partial_\mu G^a_\nu - \partial_\nu G^a_\mu - g_s f^{abc}G^b_\mu G^c_\nu \\ W^i_{\mu\nu} &= \partial_\mu W^i_\nu - \partial_\nu W^i_\mu - g\epsilon^{ijk}W^j_\mu W^k_\nu \\ B_{\mu\nu} &= \partial_\mu B_\nu - \partial_\nu B_\mu \end{aligned}$$

where f^{abc} and ϵ^{ijk} are the group structure constants of SU(3) and SU(2), respectively (the strength tensor of the hypercharge field B_μ does not have this extra term since U(1) is abelian). This is the origin of gluons and electroweak bosons self-interactions.

The second line in Equation (1) describes the Higgs field and generates the masses of the weak gauge bosons $W^\pm$, Z^0 and of the Higgs boson. In particular, the term $\left|D_\mu\phi\right|^2$ generates all interactions between the gauge bosons and the Higgs field.

The third line in Equation (1) is responsible for fermion kinetic energies as well as their interactions with all bosons (gluons and eletroweak bosons). We have five terms: left-handed lepton doublets, right-handed lepton singlets (only charged leptons since right-handed neutrinos do not couple in the SM), left-handed quark doublets, right-handed up-type quark singlets and right-handed down-type quark singlets. The covariant derivative terms relative to each group apply only to these fermions that transform under that group. For instance, the first term would expand as

$$i\bar{L}\not{D}L = i\bar{L}\gamma^\mu D_\mu L = i\begin{pmatrix} \bar{\nu}^\alpha_L & \bar{e}^\alpha_L \end{pmatrix}\gamma^\mu\left(\partial_\mu - ig\frac{\sigma^i}{2}W^i_\mu - ig'\frac{Y}{2}B_\mu\right)\begin{pmatrix} \nu^\alpha_L \\ e^\alpha_L \end{pmatrix},$$

since the leptons do not carry color charge, but the fourth term would expand as

$$i\bar{u}\not{D}u = i\bar{u}\gamma^\mu D_\mu u = i\bar{u}^i_R\gamma^\mu\left(\partial_\mu - ig_s T^a G^a_\mu - ig'\frac{Y}{2}B_\mu\right)u^i_R,$$

because the right-handed quark is a singlet under $\mathrm{SU}(2)_\mathrm{L}$.

Finally, the couplings between the Higgs boson and the fermions, and in turn fermion masses, are generated by the fourth line in Equation (1). These terms are gauge invariant, but give rise to fermion masses. For example, for the leptons and taking the Higgs field expansion around ϕ_0, the first term will expand as

$$Y_e\bar{L}\phi e = \frac{Y_e^{\alpha\beta}}{\sqrt{2}}\begin{pmatrix}\bar{\nu}^\alpha_L & \bar{e}^\alpha_L\end{pmatrix}\begin{pmatrix}0 \\ v+h(x)\end{pmatrix}e^\beta_R = \frac{Y_e^{\alpha\beta}}{\sqrt{2}}\left[v+h(x)\right]\bar{e}^\alpha_L e^\beta_R$$

which in addition to its hermitian conjugate will ultimately yield the term

$$\frac{Y_e^{\alpha\beta}}{\sqrt{2}}v\left[\bar{e}^\alpha_L e^\beta_R + \bar{e}^\alpha_R e^\beta_L\right] = \frac{Y_e^{\alpha\beta}v}{\sqrt{2}}\bar{e}^\alpha e^\beta$$

after spontaneous symmetry breaking. One can easily identify the mass of the three charged leptons as

$$m_e = \frac{Y_e^{ee}v}{\sqrt{2}}, \quad m_\mu = \frac{Y_e^{\mu\mu}v}{\sqrt{2}} \quad \text{and} \quad m_\tau = \frac{Y_e^{\tau\tau}v}{\sqrt{2}}.$$

To generate mass terms for up-type like quarks the Yukawa term involves the charge conjugate of the Higgs doublet (as in the second term of the fourth line in Equation (1)).

The Standard Model Lagrangian in Equation (1) governs the interactions between all particles within the theory. These interactions can be represented as vertices in Feynman diagrams. The vertices shown in Figure 2 are all possible interactions in the SM, and are constructed from the terms in the SM Lagrangian. Terms that, after SSB, involve only two fields do not result in vertices as they are interpreted as mass terms. Consequently, we only see vertices with at least three fields.

For instance, to derive the QED vertex for the electron, one must expand the terms $i\,(\bar{L}\not{D}L + \bar{e}\not{D}e)$ and keep the terms of the form $\bar{e}\cdot\ldots\cdot e$. This expansion ultimately yields two contributions. The first one corresponds to the coupling of the electron to the photon field:

$$-\frac{gg'}{\sqrt{g'^2+g^2}}\bar{e}\gamma^\mu eA_\mu = -e\bar{e}\gamma^\mu eA_\mu\ . \tag{2}$$

The first e in the latter expression refers to the electrical charge, therefore connecting both couplings g and g' with the electrical charge and the weak mixing angle, yielding $e = g'\cos\theta_\mathrm{W} = g\sin\theta_\mathrm{W}$. The second term that arises corresponds to the Z^0 boson:

$$\frac{1}{\sqrt{g'^2+g^2}}\left(\frac{g'^2-g^2}{2}\bar{e}_L\gamma^\mu e_L + g'^2\bar{e}_R\gamma^\mu e_R\right)Z^0_\mu\ .$$

We can see that the Z^0 couples to both left-handed and right-handed components of the electron but with different strengths. Hence, by removing the fields from Equation (2) and multiplying by i, the coupling of the electron to the photon associated with the QED vertex is

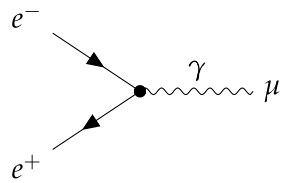

$$= -ie\gamma^{\mu} \ . \tag{3}$$

Each of the vertices in Figure 2 has an associated factor that can be computed from the SM Lagrangian density in a similar manner. Therefore, we can observe, for example, that the Higgs boson does not couple to the photon or the gluon field, and that there is no direct interaction between three fermions.

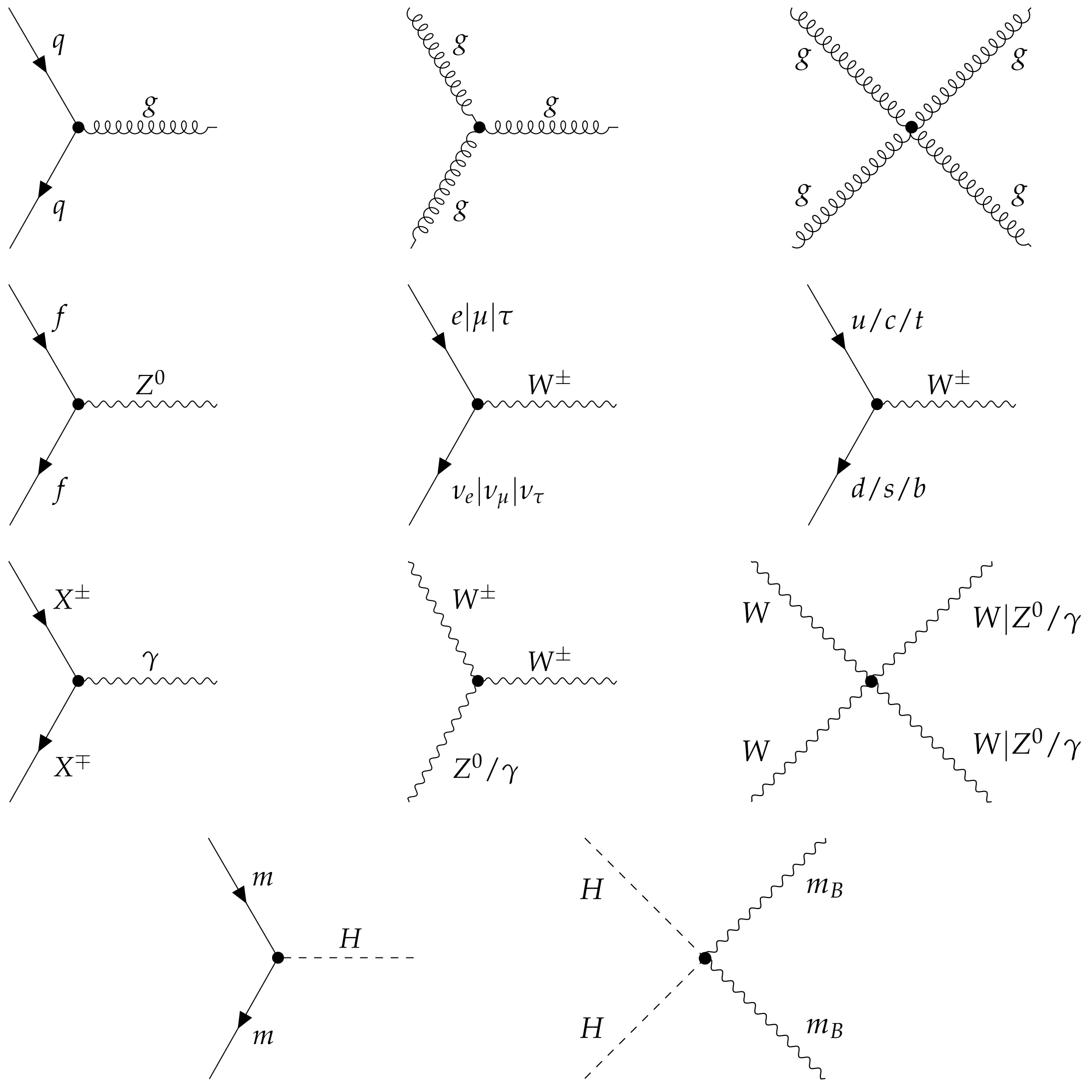

Figure 2: All possible interactions in the Standard Model, represented by Feynman diagrams. q is any quark, g is (any) gluon, $X^{\pm}$ is any charged particle, γ is a photon, f is any fermion, m is any massive particle (except neutrinos), m_B is any massive boson. In diagrams with multiple particle labels separated by / one particle label is chosen. In diagrams with particle labels separated by | the labels must be chosen in the same order. For example, in the four electroweak boson case the valid diagrams are $WWWW$, $WWZZ$, $WW\gamma\gamma$ and $WWZ\gamma$.

The Standard Model has proven to predict numerous measurements with exceptional precision. Yet, the theory does not explain why the masses of all particles are given by the values we measure. In fact, aside from the mass of the photon, which is protected by the unbroken U(1) gauge symmetry of QED, the SM does not predict any other mass value. All fermion masses (or equivalently, the Yukawa couplings) are free parameters of the theory.

While this theory has been remarkably successful, it cannot serve as the final theory of nature, as numerous unresolved puzzles persist. Many cosmological observations remain unaccounted for by the SM, such as the baryon-antibaryon asymmetry, the behaviour of gravity as described by General Relativity, the accelerated expansion of the Universe — potentially described by dark energy — and the absence of a suitable candidate for dark matter. Furthermore, the SM fails to explain the non-vanishing mass of the neutrinos as a consequence of neutrino flavour oscillation. In pursuit of a superior theory capable of encompassing the SM as well as these (and many other) discrepancies, the physics community is thoroughly trying to "break" the Standard Model to unveil hints towards an ultimate theory.

1.2 The Higgs boson

In 1964, Peter Higgs, along with five other theoretical physicists, proposed the Higgs mechanism to explain how certain particles (fermions and weak bosons) might acquire mass in local gauge theories [4, 5, 6]. If these ideas were correct, a spin-0 particle (namely the Higgs boson) should exist and possess some well-defined properties. Nearly 50 years later, on the 4^{th} of July 2012, a scalar particle consistent with the Higgs boson was discovered at the LHC by the CMS and ATLAS collaborations [7, 8].

1.2.1 Properties of the Higgs boson

The Higgs boson is a weak isospin $SU(2)_L$ doublet, massive scalar neutral boson. Table 1 summarizes the SM predicted properties [9, 10] as well as the measured properties of the Higgs boson from the Particle Data Group (PDG) [11].

Property	SM prediction	Mesasured value
Mass	$m \lesssim 700$ GeV	$m = 125.25 \pm 0.17$ GeV
Spin	$J = 0$	$J = 0$
Electric charge	$q = 0$	$q = 0$
Full width	$\Gamma = 4.12 \pm 0.06$ MeV	$\Gamma = 3.2^{+2.8}_{-2.2}$ MeV
Lifetime	$\tau = (1.60 \pm 0.02) \times 10^{-22}$ s	$\tau = 2.1^{+4.5}_{-1.0} \times 10^{-22}$ s

Table 1: Properties of the Higgs boson. The SM prediction for the full width and the lifetime depend on the Higgs mass, which is assumed to be $m = 125.25$ GeV.

As stated previously, the SM does not predict the mass of any particle (except for the photon), including the mass of the Higgs boson. Nevertheless, some theoretical arguments, such as radiative corrections and unitarity considerations, enabled theorists to establish upper bounds on the Higgs mass [9].

1.2.2 Main production modes of the Higgs boson

To understand the production and decay modes of the Higgs boson, it's important to recall that the Higgs boson couples to all the other massive particles of the SM (it couples to the gauge bosons via the $\left|D_\mu \phi\right|^2$ term in the Higgs part of the SM Lagrangian and to fermions via the Yukawa couplings), as well as to itself. Expanding the terms in the Lagrangian reveals that the coupling between the Higgs boson and any fermion is directly proportional to the particle's rest mass, while the coupling between the Higgs boson and any massive vector boson is directly proportional to the square of the particle's rest mass.

Collecting the relevant Feynman vertices, one can determine the dominant production modes for the Higgs boson, as shown in Figure 3. Since the heavier the particle, the stronger its Higgs coupling constant is, we observe that in most cases, the particles involved in the vertex where the Higgs boson is produced are very heavy (top and bottom quarks and massive gauge bosons).

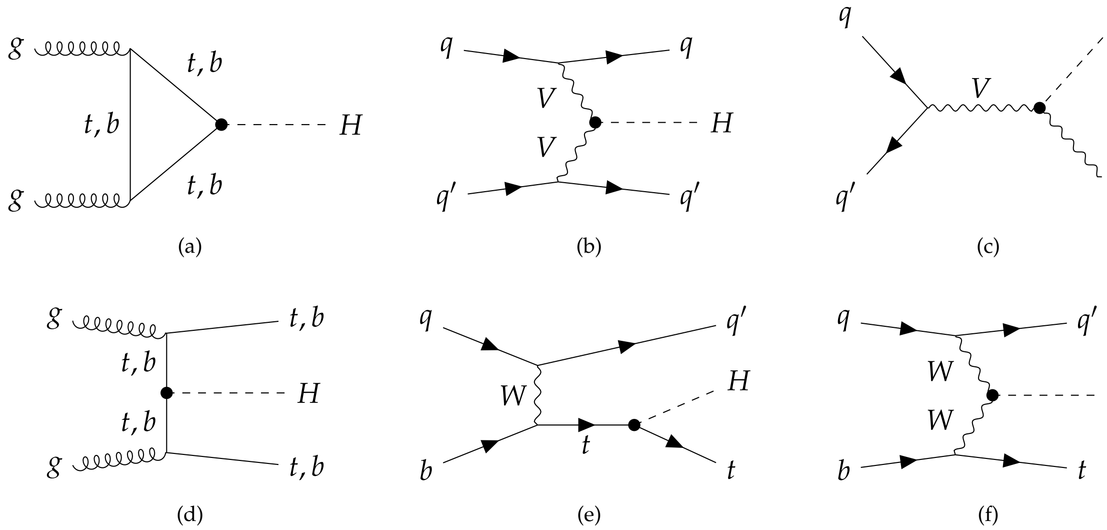

Figure 3: Higgs boson production in (a) gluon-gluon fusion (ggH), (b) vector boson fusion (VBF), (c) associated production with a W or Z (V) boson (VH), also known as Higgsstrahlung, (d) associated production with a top or bottom quark pair (ttH or bbH), or tt fusion, and (e, f) associated production with a single top quark (tH).

Despite being a second-order process (it requires a heavy quark loop), the strong coupling to heavy quarks makes gluon fusion the process that contributes the most to the production of the Higgs boson at the LHC, a proton-proton (pp) collider. The LHC is a gluon-gluon collider when it comes to Higgs production, as gluons dominate the production of Higgs bosons with a mass of around 125 GeV. The second most important process at the LHC is vector boson fusion, where two fermions collide and exchange a virtual vector boson, which radiates a Higgs boson. The third contribution to Higgs boson production, and the first one at LEP, is associated production with a vector boson or Higgsstrahlung. In this production mode, a fermion and antifermion collide and can form a virtual $W^{\pm}$ or Z^0 boson which, if it carries enough energy, can emit a Higgs boson.

[**TODO:** Add Higgs production signatures]

To compare the different production cross sections with the SM predictions, we introduce some important quantities to describe interactions at particle colliders. The *center-of-mass* *energy* $\sqrt{s}$ describes the combined energy of the collided particle beams and is defined as the square root of the Mandelstam variable

$$\sqrt{s} = \sqrt{(p_1 + p_2)^2} \ ,$$

where p_1 and p_2 are the four-momenta of the two particles. When colliding elementary particles (e.g., e^+e^-), the center-of-mass energy is precisely the available energy to produce particles in the collision. When colliding composite particles (e.g., protons), however, the available energy to produce particles is slightly less due to the parton distribution functions within the proton, and there is an energy spread. The *cross section* σ of a process describes the likelihood of a specific final state, as a measure of the effective area or target size for a particular interaction. It is measured in units of area, usually barns, defined as barn $= 10^{-28}$ cm^2. The number of events per unit time can be expressed in terms of the *instantaneous luminosity* $\mathscr{L}$ and the cross section of the studied event σ as

$$\frac{\mathrm{d}N_{\text{events}}}{\mathrm{d}t} = \mathscr{L}\sigma \ ,$$

and the *integrated luminosity* is defined as

$$L = \int \mathscr{L} \mathrm{d}t \ .$$

Finally, the *signal strength* μ expresses a measured cross section divided by the expected SM value.

Having established these fundamental concepts, we can now compare the theoretical and measured cross sections for the production of the Higgs boson. Our analysis uses 2018 data from the LHC, with a center-of-mass energy of $\sqrt{s} = 13$ TeV and an integrated luminosity of $L = 39.54$ fb^{-1}. According to the SM and assuming $m_H = 125.25$ GeV, the total Higgs boson cross section at a center-of-mass energy of $\sqrt{s} = 13$ TeV is $\sigma = 55500 \pm 2800$ fb [10], with around 87% coming from gluon fusion, 7% from vector boson fusion and 4% from Higgsstrahlung. The predicted and measured cross section of the Higgs boson at $\sqrt{s} = 13$ TeV from different production modes are shown in Table 2.

Production mode	SM σ [fb]	Measured σ [fb]	Measured μ
ggH	48400 ± 2440	47000 ± 4500	0.97 ± 0.08
VBF	3774 ± 81	3020 ± 460	0.80 ± 0.12
WH	1365 ± 28	2030 ± 360	1.49 ± 0.26
Z^0H	879 ± 36	1130 ± 220	1.29 ± 0.24
ttH + H	582 ± 61	660 ± 130	1.13 ± 0.18
bbH	484 ± 116	-	-

Table 2: Cross section of the Higgs boson's most frequent production modes at $\sqrt{s} = 13$ TeV. SM values from Ref. [10], measured μ values from Ref. [12], and measured σ from $\sigma = \mu\sigma_{\text{SM}}$. At the moment of this writing, the bbH production channel has not been measured yet.

Since the most significant Higgs boson production channel is gluon fusion, within the limited timeframe of this project, our primary focus will be on this production mode. However, other modes, such as vector boson fusion or associated production with a W/Z boson, share reasonable similarities with ggH in terms of implementation and could be further extensions of this analysis.

1.2.3 Main decay channels of the Higgs boson

The Higgs boson is a very short-lived particle, decaying almost instantaneously after its production into lighter particles. According to the couplings of the Higgs field to all other SM particles, at the first loop order, the Higgs boson predominantly decays to the most massive particles that are kinematically accessible. However, there are certain decay modes where the Higgs boson decays into massless particles, such as gluon or photon pairs, as the first-loop contributions are not negligible. Figure 4 shows the most relevant Feynman diagrams for the Higgs boson decay, while Table 3 presents the most frequent decay channels for the Higgs boson, comparing the SM predicted value to the measured value for every decay mode.

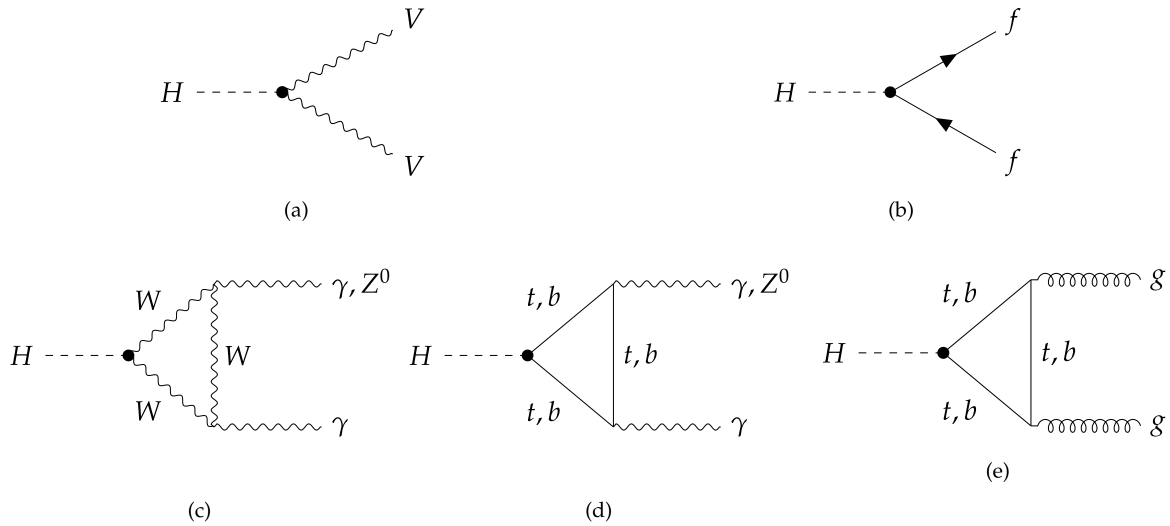

Figure 4: Higgs boson decays into (a) heavy vector boson pairs (V is $Z^0/W^{\pm}$), (b) fermion-antifermion pairs, (c, d) photon pairs or $Z^0\gamma$, and (e) gluon pairs.

Decay channel	SM $\mathcal{B}$ (%)	Measured $\mathcal{B}$ (%)	Measured μ
$\mathrm{H} \longrightarrow b\bar{b}$	57.8 ± 0.7	60 ± 12	1.04 ± 0.20 [13]
$\mathrm{H} \longrightarrow WW^*$	21.8 ± 0.3	20.7 ± 2.1	0.95 ± 0.09 [14]
$\mathrm{H} \longrightarrow gg$	8.2 ± 0.4	-	-
$\mathrm{H} \longrightarrow \tau^+\tau^-$	6.23 ± 0.10	6.1 ± 1.1	0.98 ± 0.18 [15]
$\mathrm{H} \longrightarrow c\bar{c}$	2.87 ± 0.16	< 40	< 14 [16]
$\mathrm{H} \longrightarrow ZZ^*$	2.68 ± 0.04	2.6 ± 0.3	0.97 ± 0.12 [12]
$\mathrm{H} \longrightarrow \gamma\gamma$	0.227 ± 0.005	0.254 ± 0.021	1.12 ± 0.09 [17]
$\mathrm{H} \longrightarrow Z\gamma$	0.155 ± 0.009	0.37 ± 0.14	2.4 ± 0.9 [18]
$\mathrm{H} \longrightarrow s\bar{s}$	0.025 ± 0.001	-	-
$\mathrm{H} \longrightarrow \mu^+\mu^-$	0.0216 ± 0.0004	0.026 ± 0.009	1.19 ± 0.43 [19]

Table 3: Most frequent decay modes of the Higgs boson. SM values from Ref. [10, 12], and measured $\mathcal{B}$ from $\mathcal{B} = \mu\mathcal{B}_{\mathrm{SM}}$. At the moment of this writing, the $\mathrm{H} \longrightarrow gg$ and $\mathrm{H} \longrightarrow s\bar{s}$ decay channels have not been measured yet.

The predicted values by the SM in Table 3 are of significant interest, and there are some remarks worth mentioning.

Firstly, it is observed that there is no decay $\mathrm{H} \longrightarrow t\bar{t}$. This is because the Higgs boson is lighter than the top quark, $M_H = 125$ GeV $< m_t = 173$ Gev, making it not massive enough to produce a top-antitop quark pair. In fact, the Higgs boson can not even create one real top quark and one virtual top quark. Consequently, the presence of top quarks in the Higgs boson decays is limited to virtual loops, as the ones present in diagrams (d) and (e) of Figure 4.

Let us examine the branching ratios in Table 3 more closely, starting with the fermionic decays. The Higgs-fermion vertex has a factor of

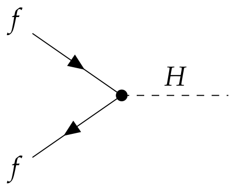

$$= -i\frac{m_f}{v}\ , \tag{4}$$

thus at first approximation, the expected decay width at tree level can be estimated as proportional to

$$\Gamma(H \to f\bar{f}) \propto N_C m_f^2\ , \tag{5}$$

where N_C is the number of colours (3 for quarks, 1 for leptons). It is important to note that the mass to use in the above expression is the *running mass* of the particle at an energy scale of $\mu = M_H$, rather than the ones presented in Figure 1[1]. Using the running masses of the particles (for precise values of the running masses, see Ref. [20]) and the approximation presented above, we obtain the following relation of decay widths for the quarks, taking $\Gamma(H \to s\bar{s}) = 1$:

$$\Gamma(H \to b\bar{b}) : \Gamma(H \to c\bar{c}) : \Gamma(H \to s\bar{s}) \approx 2834 : 136 : 1\ ,$$

while the full SM computation yields

$$\Gamma(H \to b\bar{b}) : \Gamma(H \to c\bar{c}) : \Gamma(H \to s\bar{s}) = 2312 : 115 : 1\ .$$

The approximation in Equation (5) is even better for leptons:

$$\Gamma(H \to \tau^+\tau^-) : \Gamma(H \to \mu^+\mu^-) \approx 288.53 : 1\ ,$$

while the full SM computation is remarkably close, giving

$$\Gamma(H \to \tau^+\tau^-) : \Gamma(H \to \mu^+\mu^-) = 288.43 : 1\ .$$

The discrepancies between this initial approximation and the results from the SM in Table 3 arise from phase space factors, higher-order Feynman diagrams, and, in the case of quarks, QCD corrections.

For vector bosons, the vertex has a factor of

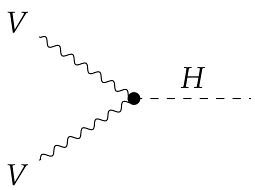

$$= 2i\frac{M_V^2}{v}g^{\mu\nu}\ , \tag{6}$$

[1]The masses of the quarks that are typically provided, for example, in Ref. [11], are $m_u(\mu = 2\text{ GeV})$, $m_d(\mu = 2\text{ GeV})$, $m_s(\mu = 2\text{ GeV})$, $m_c(\mu = m_c)$, $m_b(\mu = m_b)$. The t-quark mass is determined from event kinematics, see Ref. [11]. The differences in the masses at the Higgs energy scale compared to the "usual" values are more pronounced for heavy quarks. For more information on running masses refer to Ref. [20].

and similarly, one can estimate the expected decay width at tree level as proportional to

$$\Gamma(H \to VV) \propto M_V^4 \ . \tag{7}$$

When we compute the same relations as for the fermions we obtain

$$\Gamma(H \to WW^*) : \Gamma(H \to ZZ^*) \approx 0.604 : 1 \ ,$$

while the full SM computation differs by almost a factor of 14:

$$\Gamma(H \to WW^*) : \Gamma(H \to ZZ^*) = 8.134 : 1 \ .$$

Despite the vertex in Equation (6) suggesting that $\Gamma(H \to WW^*) < \Gamma(H \to ZZ^*)$ due to $M_W < M_Z$, other factors play a more significant role in the decay width than just the vertex factors in the boson decays. First of all, the phase space of the decay into Z^0 bosons includes an extra $\frac{1}{2}$ symmetry factor due to the decay involving two identical particles. The remaining factor of 7 arises from the inclusion of higher-order Feynman diagrams and, most significantly, from the phase space contribution. The latter contribution quantifies the number of valid momentum and energy configurations for the outgoing particles while still obeying the conservation of energy and momentum.

Note that $2M_W, 2M_Z > M_H > M_W, M_Z$, so for the Higgs boson to decay into two electroweak bosons, one of them must be *off-shell* or *virtual* (that is why one of them is marked with an asterisk). Off-shell or virtual particles do not need to satisfy the equation $E^2 - p^2 = m^2$, and are very short-lived. Therefore, for instance, the decay $H \to WW^*$ means that the Higgs boson decays into a real W boson and a virtual W^* boson, which immediately decays into other particles. The phase factor for such a decay is intricate, as it involves the decay of a virtual boson into all possible channels, but is much smaller than it would be if the Higgs could decay to two real Z^0 or $W^\pm$ bosons. Additionally, the phase space contribution for the ZZ^* channel is much smaller than that for the WW^*. This is mainly because the invariant mass of the virtual Z^0 boson tends to deviate more from the real Z^0 mass than the virtual $W^\pm$ boson is from the real $W^\pm$ mass.

There are two decaying channels in Table 3 that have not yet been experimentally tested. The H $\to s\bar{s}$ channel is extremely challenging to measure due to its low branching fraction, which is more than two orders of magnitude smaller than that of the $c\bar{c}$ channel, for which only an upper bound is currently known. The other channel, accounting for approximately 8% of the Higgs boson decays, is the decay into a pair of gluons. Experimentally determining this branching ratio at the LHC is incredibly difficult because it involves QCD processes that are almost indistinguishable from the QCD background present at the Large Hadron Collider.

Additionally, the Higgs boson decays into massless particles (gluons and photons) account for one in 12 decays. This indicates that, despite being higher-order Feynman diagrams, heavy quark loops, mainly involving top and bottom quarks, are not negligible and compete with tree-level decays. The decay into a pair of photons is particularly interesting because its signature in hadron colliders is relatively clean compared to the hadronic background, and was used in the Higgs boson discovery at the LHC in 2012.

1.3 Searching of a model beyond the SM

If the Standard Model is correct, the coupling between the Higgs boson and each massive fermion (boson) is directly proportional to the fermion's mass (the square of the boson's mass), as shown in Equations (4) and (6). One can visualize these relationships by plotting the Higgs couplings against the masses of the particles. According to the SM, this should result in a linear relationship, as in Figure 5.

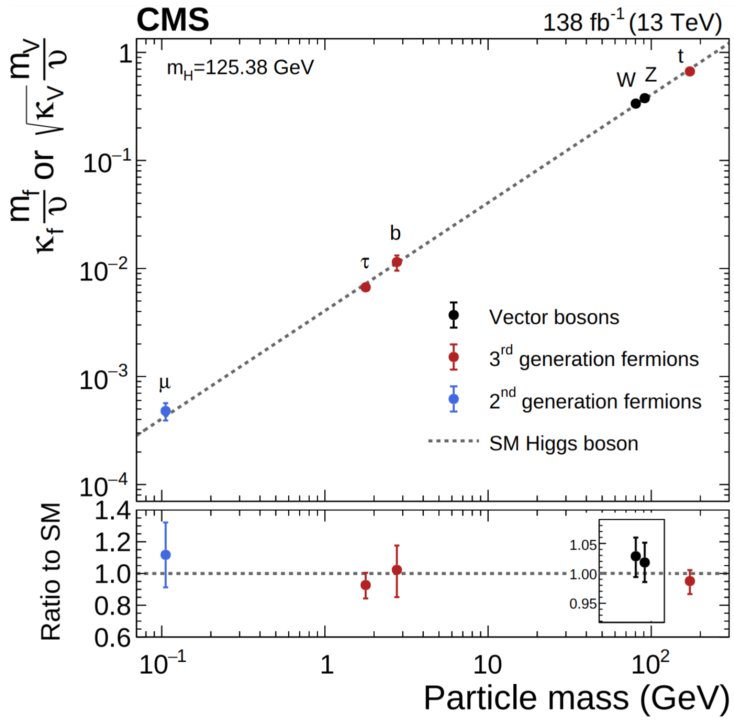

Figure 5: Relationship between the Yukawa couplings of the third-generation fermions, massive bosons, and the second-generation muon and its masses, from Ref. [12]. The dashed straight line represents the Standard Model prediction.

As of the time of writing, the measured values for the massive weak bosons, the third generation of fermions (top and bottom quarks and the tau lepton), as well as the second-generation lepton (the muon), align remarkably well with the Standard Model predictions, as seen in Figure 5. This exceptional agreement with the predictions of the Higgs mechanism, spanning three orders of magnitude in mass, is a powerful test of the validity of the underlying physics.

To further test the validity of the SM, it is interesting to expand the plot to include lighter fermions, specifically the second-generation strange and charm quarks, as well as all first-generation fermions, including the up and down quarks and the electron. Additionally, the non-vanishing masses of the neutrinos may suggest a Yukawa-type coupling for them as well.

Direct searches for Higgs boson decays into charm pairs have been conducted by both the ATLAS and CMS collaborations. Additionally, searches for $\mathrm{H} \rightarrow e^+e^-$ have been carried out to complete the picture. Furthermore, both collaborations have explored potential Beyond the Standard Model (BSM) couplings of the Higgs boson, including searches for flavour-changing neutral currents via t-quark decays ($t \rightarrow cH$ and $t \rightarrow uH$), as well as lepton flavour-violating decays such as $H \rightarrow e^{\pm}\mu^{\mp}$, $H \rightarrow e^{\pm}\tau^{\mp}$ and $H \rightarrow \mu^{\pm}\tau^{\mp}$. To date, no evidence supporting these couplings has been found.

Currently, the couplings of light quarks (u, d, s) to the Higgs boson remain loosely constrained by the existing data on the total Higgs boson width. The large multi-jet background at the LHC inhibits the study of such couplings with inclusive $H \rightarrow q\bar{q}$. Rare exclusive decays of the Higgs boson into a light meson and a photon have been proposed as a probe of both flavor-conserving and flavor-violating couplings of the Higgs boson to light quarks (up, down, charm and strange). Exclusive decays involving $W^{\pm}$ and Z^0 bosons are also a possibility [21].

Initial experimental upper limits on hadronic two-body Higgs decays have been established by the ATLAS and CMS collaborations (ATLAS-CMS: $H \rightarrow J/\psi + \gamma$ [22, 23], ATLAS: $H \rightarrow \rho, \phi, \omega, K^{*0} + \gamma$ [24, 25], CMS: $H \rightarrow J/\psi, \rho, \phi + Z^0$ [26, 27]).

This analysis focuses on decays of the form $H \rightarrow M\gamma$, where M represents a light vector meson with a mass of approximately 1-2 GeV. It is important to note that, given that the Higgs boson has spin 0 and the photon has spin 1, the meson M must be a *vector* meson to conserve total angular momentum.

Table 4 presents exotic decays of this form. The first three rows involve similar processes in which the vector meson decays into a pair of lighter, charged scalar mesons. These processes are currently under analysis by a group within the CMS collaboration as of the writing of this document. However, our specific focus within this analysis lies in the lower half of the table, where the vector meson decay involves a pair of charged scalar mesons along with neutral particles, specifically either pions or photons.

Higgs boson rare decay	Coupling
$H \rightarrow \rho^0\gamma$ $\hookrightarrow \pi^+\pi^-$ (∼100%)	up/down quark
$H \rightarrow \phi\gamma$ $\hookrightarrow K^+K^-$ (49.1±0.5%)	strange quark
$H \rightarrow K^{*0}\gamma$ $\hookrightarrow K^{\pm}\pi^{\mp}$ (∼100%)	flavor-violating down/strange quark
$H \rightarrow \phi\gamma$ $\hookrightarrow \pi^+\pi^-\pi^0$ (15.4±0.4%)	strange quark
$H \rightarrow \omega\gamma$ $\hookrightarrow \pi^+\pi^-\pi^0$ (89.2±0.7%)	up/down quark
$H \rightarrow D^{*0}\gamma$ $\hookrightarrow D^0 + \pi^0/\gamma$ (∼100%) $\hookrightarrow K^{\mp}\pi^{\pm}$ (3.962±0.031%) $\hookrightarrow K^{\mp}\pi^{\pm}\pi^0$ (14.43±0.50%)	flavor-violating up/charm quark

Table 4: Higgs rare decays of the form $H \longrightarrow M\gamma$, where M is a vector meson containing light quarks. The top half of the table focuses on decays where the light neutral vector meson decays into a pair of charged mesons. The bottom half of the table focuses on similar decays, but where there are also one or two neutral particles involved in the decay of the primary meson. All these decays are currently being analised by the Particle Physics Collaboration (PPC) at MIT within the CMS collaboration. The branching ratios of meson decays are shown in parenthesis, from the PDG [11].

The current branching ratio information of these decays known at the moment of this writing, both theoretical and experimental, is shown in Table 5. For the first three decays

Decay channel	SM $\mathcal{B}$		Measured $\mathcal{B}$	
$\mathrm{H} \longrightarrow \rho^0\gamma$	$(1.68 \pm 0.08) \times 10^{-5}$	[28]	$< 8.8 \times 10^{-4}$	[24]
$\mathrm{H} \longrightarrow \phi\gamma$	$(2.31 \pm 0.11) \times 10^{-6}$	[28]	$< 4.8 \times 10^{-4}$	[24]
$\mathrm{H} \longrightarrow \omega\gamma$	$(1.48 \pm 0.08) \times 10^{-6}$	[28]	$< 1.5 \times 10^{-4}$	[25]
$\mathrm{H} \longrightarrow K^{*0}\gamma$	$< 10^{-11}$	[25]	$< 8.9 \times 10^{-5}$	[25]
$\mathrm{H} \longrightarrow D^{*0}\gamma$	-		-	

Table 5: Higgs rare decay branching fractions. Because of the very large hadronic background at the LHC, only upper limits on the branching ratios have been computed so far, which are around two orders of magnitude bigger than the SM prediction. The $\mathrm{H} \longrightarrow D^{*0}\gamma$ channel has not been measured yet.

in Table 5, the measured upper limits are 52, 208 and 95 times the expected SM values, respectively. For the $\mathrm{H} \longrightarrow K^{*0}\gamma$ decay, only $\mathcal{B}(\mathrm{H} \longrightarrow d\bar{s} + \bar{d}s)$ is available, with a value of $\mathcal{B}(\mathrm{H} \longrightarrow d\bar{s} + \bar{d}s) = 1.19 \times 10^{-11}$ [29]. However, $\mathcal{B}(\mathrm{H} \longrightarrow K^{*0}\gamma)$ is expected to be much smaller [25]. A similar situation occurs for the last decay, where only $\mathcal{B}(\mathrm{H} \longrightarrow c\bar{u} + \bar{c}u)$ is available, with a value of $\mathcal{B}(\mathrm{H} \longrightarrow c\bar{u} + \bar{c}u) = 5.00 \times 10^{-20}$ [29].

When studying Higgs boson decays of the form $\mathrm{H} \longrightarrow M\gamma$, which in essence are $\mathrm{H} \longrightarrow q\bar{q}\gamma$, there are different Feynman diagrams that contribute to the width. We can distinguish the contributions into two different vertices. On the one hand, we have the tree-level diagram, which provides the direct contribution and is shown in diagram (a) of Figure 6. On the other hand, we have all other higher-order diagrams joined as an effective indirect vertex, represented in diagram (b) of Figure 6.

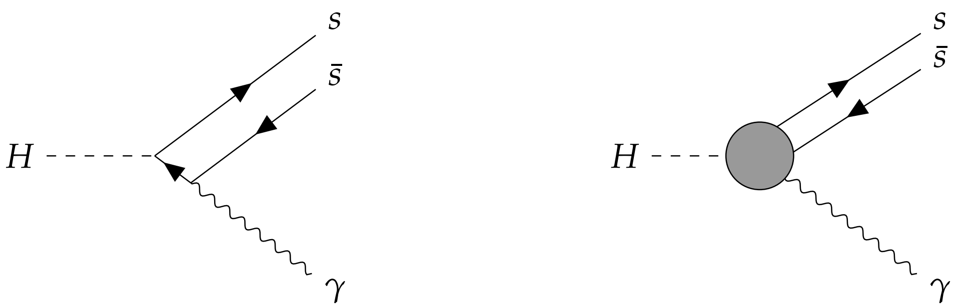

(a) (b)

Figure 6: Direct (a) and indirect (b) contributions involved in the decays under analysis. Here we have considered the decay to a strange-antistrange quark pair, but it is analogous for the other light quarks.

According to the Standard Model, the direct contribution is of the order of 10^{-11}, while the indirect contribution is of the order of 10^{-6}, which means that higher-order corrections dominate the behaviour of these type of decays.

A few examples of diagrams that contribute to the effective vertex are provided in Figure 7. In diagram (a) the blue loop can either be a heavy charged fermion loop or a $W^{\pm}$ boson loop.

To ultimately compute the Yukawa couplings to the lighter families of quarks, one has to take into consideration contributions from both the direct and the indirect vertex, since experimentally what is measured from the direct decay is the overall effect coming from both

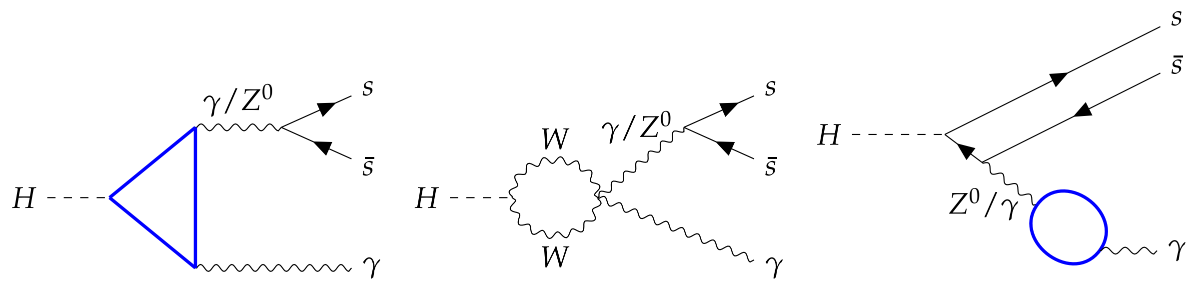

Figure 7: Some examples of the many one-loop diagrams accounted for in the effective vertex. The blue loops are heavy charged fermion or $W^{\pm}$ boson loops.

vertices.

Therefore, the full diagrams of the decays that are object of study in these thesis (bottom half part of Table 4) are shown in Figure 8.

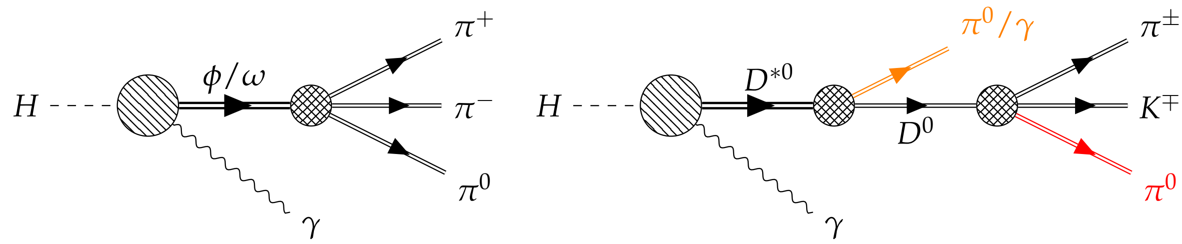

Figure 8: Full diagrams of the Higgs rare decays studied. Diagram (a) shows the decays H $\longrightarrow \phi/\omega\gamma$. Diagram (b) shows the different decays H $\longrightarrow D^{*0}\gamma$, where the orange line indicates that the particle can either be a π^0 ($\sim$ 65%) or a γ ($\sim$ 35%) [11]. This last diagram includes the two decays involving D^{*0} studied, where π^0 is not there for the 2-body decay of the D^0 meson.

Diagram 8 (a) depicts the decays H $\longrightarrow \phi\gamma$ and H $\longrightarrow \omega\gamma$, which are very similar and are going to share a lot of the features of the framework built. Diagram 8 (b) shows the decays involving a D^{*0} meson, H $\longrightarrow D^{*0}\gamma$, where the orange line from the decay of the D^{*0} meson indicates that the particle can either be a π^0 (in around 65% of the cases) or a γ ($\sim$ 35%) [11]. This diagram encompasses the two decays involving D^{*0} studied, where $D^0 \longrightarrow K^{\mp}\pi^{\pm}$ corresponds to the diagram where the red line associated to π^0 is removed, and $D^0 \longrightarrow K^{\mp}\pi^{\pm}\pi^0$ where the red edge is maintained. It is worth noting that $D^0 \longrightarrow K^{\mp}\pi^{\pm}(\pi^0)$ is mostly $D^0 \longrightarrow K^-\pi^+(\pi^0)$, as $D^0 \longrightarrow K^+\pi^-(\pi^0)$ is doubly Cabbibo supressed (DC) [11].

The main difference between this analysis and the one studying the three decays presented in the top half of Table 4 lies in the fact that we are dealing with 3-body decays involving neutral particles, which are more challenging to track compared to charged ones. That is why we will focus most of our attention on accurately recovering the missing neutral particles.

The main goal of this Master's Thesis is to compute a reasonable expected upper limit for the branching ratio of the aforementioned Higgs boson decays. Table 5 shows the order of magnitude of the branching fractions one would ultimately like to measure. Nevertheless, due to the large hadronic background at the LHC, analyses of this kind are targeting an upper limit rather than a precise measurement at this stage.

Deviations from the predictions of the Standard Model within the Higgs boson sector can serve as compelling indications of new physics beyond our current understanding of particle physics. The Higgs boson plays a central role in the SM by giving particles mass through the Higgs mechanism. Therefore, any discrepancies in its properties, including decay widths, could reveal hidden phenomena and particles that the SM fails to describe.

One possible scenario involves determining an upper limit on a Higgs decay branching ratio that significantly exceeds the SM prediction. Such a discrepancy would suggest the presence of additional particles and interaction processes not accounted for in the SM. These new BSM particles could contribute to the Higgs decay width in ways not initially anticipated.

Accurate measurements are essential in this context, as they allow us to probe the Higgs sector with the highest level of precision. Through the precise determination of the Higgs boson's properties, one can identify even the most subtle deviations from the SM, providing clues about the nature of new physics. Consequently, the need for precision in Higgs boson measurements is of utmost importance, as it can not only further confirm the validity of the SM but also has the potential to illuminate the path towards a more comprehensive theory of particle physics, one that goes beyond the boundaries of the Standard Model.

The Future Circular Collider (FCC) project, with its proposed scenarios, including FCC-ee (electron-positron collisions) and FCC-hh (hadron-hadron collisions), presents a promising opportunity to advance our understanding of the Higgs boson and, by extension, the Standard Model [30]. The FCC-ee, with its high-energy lepton collisions, would enable us to conduct precise measurements of the Higgs boson's properties, including its interactions with other SM particles. This collider could provide an order of magnitude improvement in accuracy compared to current experiments, allowing for detailed studies of the Higgs, $W^{\pm}$, and Z^0 bosons, as well as the top quark [31, 32]. Together with the FCC-hh, which would operate with hadron collisions at significantly higher energies (potentially up to 30 times that of the current LHC [33]), these colliders within the FCC project hold the potential to shed light on dark matter, probe neutrino masses, and investigate other unexplained phenomena.

Chapter 2

The CMS at the LHC

This chapter will provide an overview of the European Organization for Nuclear Research, commonly known by its acronym CERN (Conseil Européen pour la Recherche Nucléaire), along with the Large Hadron Collider (LHC) and the Compact Muon Solenoid (CMS) experiment. It will go through the most significant breakthroughs at CERN, with a particular emphasis on the discovery of the Higgs boson at the LHC in 2012 by the CMS and ATLAS collaborations [7, 8].

2.1 The Large Hadron Collider at CERN

The European Organization for Nuclear Research (CERN) is an intergovernmental organization composed of 23 member states that operates the world's largest particle physics laboratory. Established in 1954, CERN is situated on the Franco-Swiss border near Geneva, Switzerland, and is one of the largest and most influential research organizations in particle physics. The missions of CERN include world-class research in fundamental physics, sustainable and environmentally responsible accelerator facilities, global collaboration in science and technology advancement and the education and engagement of future scientists, engineers and the broader public.

CERN has been home to many accelerators, including the original linear accelerator Linac1 (in operation from 1959 until 1992), the Linac2 (1978 - 2018), the Super Proton-Antiproton Synchrotron (S$p\bar{p}$S) (1981-1991), the Large Electron-Positron Collider (LEP) (1989-2000), and the current Large Hadron Collider (LHC), which was constructed between 1998 and 2008 and achieved its first collisions in 2010. The Future Circular Collider (FCC) is proposed to be the successor of LHC at CERN [30].

During its nearly 70-year history since its creation, many important achievements in particle physics have been made through experiments at CERN, including:

- The discovery of neutral currents by studying neutrinos produced by the PS/SPS neutrino beam interacting in the Gargamelle bubble chamber in 1973 [34].
- The discovery of the $W^{\pm}$ and Z^{0} bosons in the UA1 and UA2 experiments in 1983 [35, 36].

- The determination of the number of light neutrino families at LEP in 1989 [37].
- The discovery of direct CP violation in the NA48 experiment in 1999 [38].
- The discovery of the Higgs boson at LHC by the CMS and ATLAS collaborations in 2012 [7, 8].

Today, the main particle accelerator at CERN is the LHC. The Large Hadron Collider (LHC) is a hadron collider primarily used for proton-proton (pp) collisions but also capable of heavy-ion collisions. It was designed to investigate the properties of the Standard Model, in particular the Higgs boson, and to study the physics Beyond the Standard Model by analysing discrepancies in the SM or via direct searches of particles. It has a circumference of 26.659 kilometers and is located underground at depths ranging from 50 to 175 meters, making it the world's largest and highest-energy particle collider [39, 40].

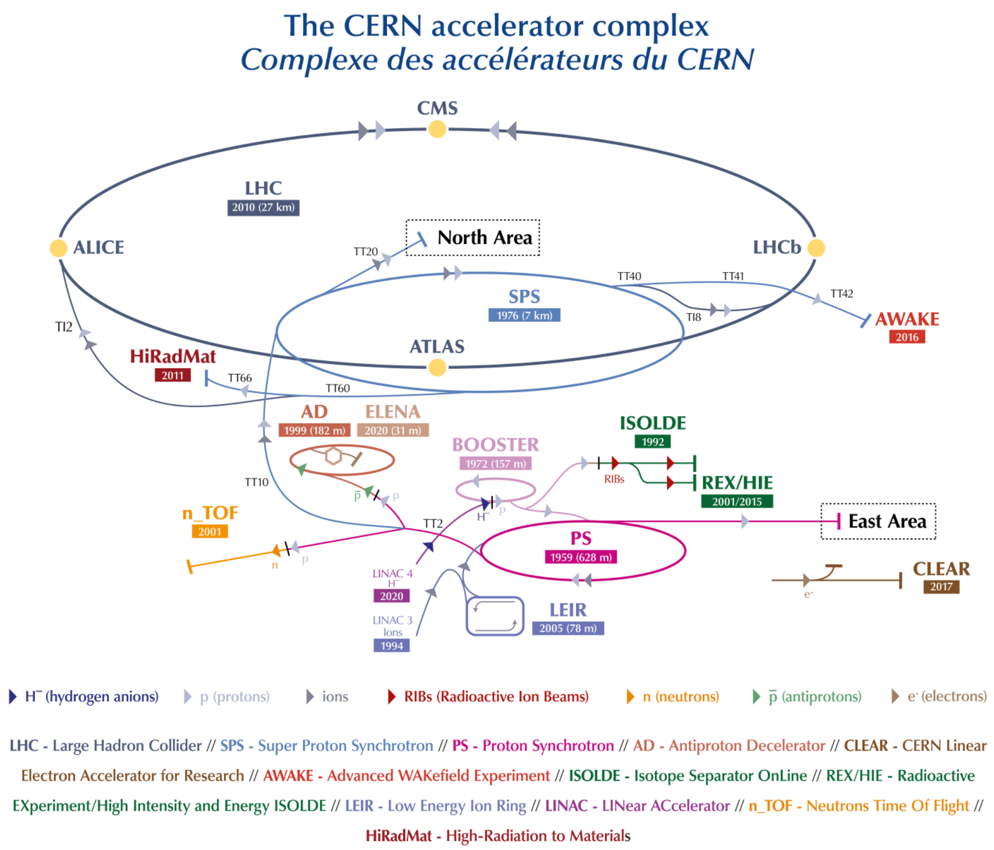

Figure 9: The CERN accelerator complex. The four main experiments can be seen in four different points around the LHC. Source: Ref. [41].

Two beams circulate in opposite directions within the LHC, guided by 9593 superconducting magnets. Operating at a center-of-mass energy of $\sqrt{s} = 13$ TeV, protons from each beam have an energy of 6.5 TeV and complete about 11245 orbits around the collider's circumference every second. This is achieved by initially stripping hydrogen atoms of their electrons, leaving the protons. Several accelerators are used in sequence to accelerate these protons: first, Linac2 (Linac4 after 2020) accelerates them to 50 MeV, followed by the Proton Synchrotron

Booster (PSB) accelerating them further to 1.4 GeV, the Proton Synchrotron (PS) to 25 GeV, and finally, the Super Proton Synchrotron (SPS), where they reach 450 GeV. The beams are then injected into the LHC, which takes them to 6.5 TeV using superconducting dipole magnets, cooled to 1.9 K with superfluid helium, producing a magnetic field of 8.3 T, and eight radio frequency (RF) cavities per beam. By tuning the energy of the protons that have a different timing than that of the RF cavity, the phase oscillations of the electromagnetic fields within these RF cavities divide the protons into 2808 bunches, each containing about 1.15×10^{11} protons. The collisions resulting from this process occur approximately every 25 ns, equivalent to a frequency of 40 MHz. These collisions take place at four interaction points, where the four major LHC experiments are located: ATLAS (A Toroidal LHC ApparatuS) [42], CMS (Compact Muon Solenoid) [43], ALICE (A Large Ion Collider Experiment) [44], and LHCb (Large Hadron Collider beauty) [45]. Of these four experiments, ATLAS and CMS are multipurpose detectors designed to study a wide range of physics phenomena. ALICE is specifically conceived to record the collisions of ion beams, while LHCb is optimized for studying b-physics. Moreover, several smaller experiments at the LHC focus on more specific physics goals. Figure 9 shows a diagram of CERN's Accelerator Complex.

One of the main advantages of LHC being a proton-proton collider, rather than an electron-positron collider like its predecessor LEP, is that it suffers much less from the effects of synchrotron radiation. This effect causes charged accelerated particles to lose energy, inversely proportional to the fourth power of the particle mass, making proton-proton collisions more energy efficient for a 13 TeV regime.

During Run 1 of the LHC, which spanned from 2010 to 2012, the center-of-mass energy ranged from 7 to 8 TeV, and CMS recorded a total integrated luminosity of 29.45 fb^{-1}. Run 2 took place from 2015 to 2018, with an energy of 13 TeV, and a total integrated luminosity of 163.6 fb^{-1}. In 2022, Run 3 began and is scheduled to conclude in 2026, with an energy of 13.6 TeV. In the first year of Run 3, the total integrated luminosity reached 42 fb^{-1}, and is expected to be around 300 fb^{-1} by the end of the Run [46]. The data that is going to be used in this analysis is from the CMS collaboration and was taken in 2018 (Run 2), with $\sqrt{s} = 13$ TeV and an integrated luminosity of 39.54 fb^{-1}.

2.2 The Compact Muon Solenoid

One of the four large particle detectors at the LHC is the Compact Muon Solenoid (CMS) detector [43, 47]. It is designed to optimize the muon detection system in proton-proton collisions, featuring a cylindrical geometry, measuring 21.5 m in length and 15 m in diameter, with a total weight of approximately 14000 tonnes. It is characterized by its solenoid magnet, which generates a 4 T magnetic field used to bend charged particles to measure their transverse momentum (p_{T}).

Concentric layers of detector subsystems surround the collision point of the particle beams at the center of the detector to measure particle trajectories and their properties. These subsystems, starting from the interaction point, include the silicon tracker, the electromagnetic calorimeter (ECAL), and the hadronic calorimeter (HCAL). Beyond the superconducting solenoid magnet there is another outer HCAL and the muon system, where another magnetic field of approximately 2 T bends the muons in the opposite direction of the first magnet. Each subdetector specializes in measuring certain particles, but they work together to reconstruct events. For more detailed information refer to [48]. A full diagram of the structure of CMS is shown in Figure 10, while a cross section is presented in Figure 11.

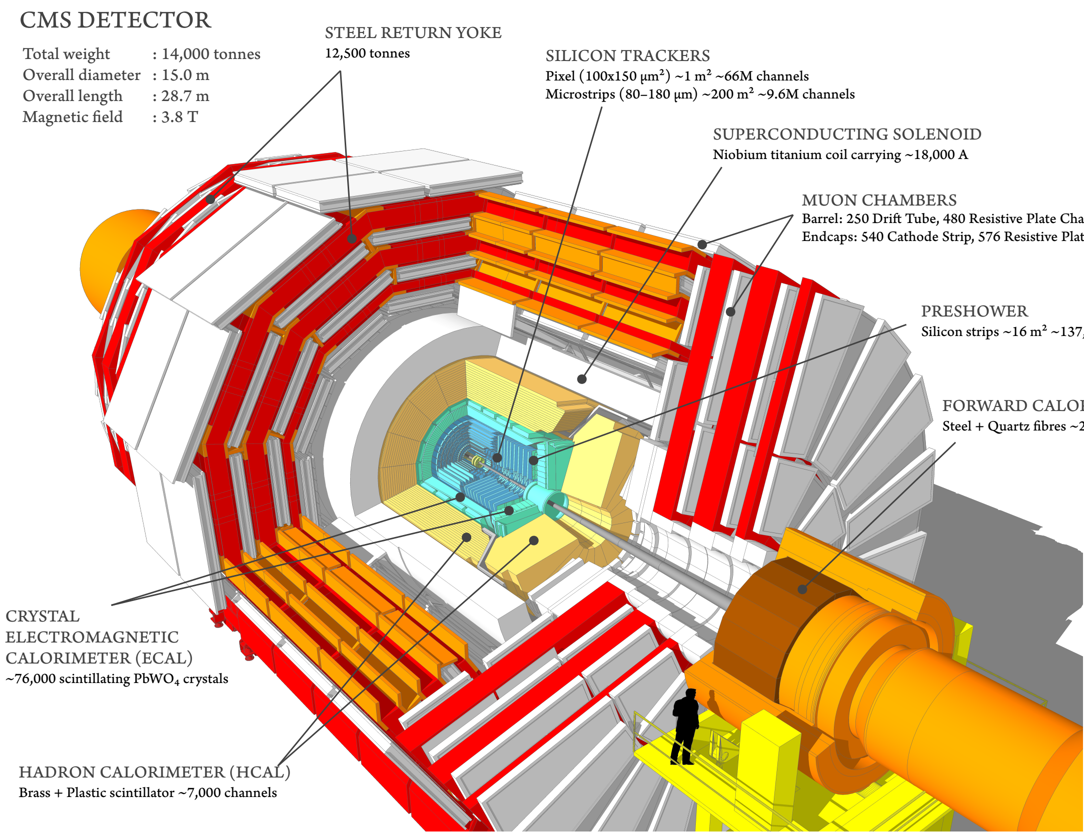

Figure 10: A cutaway view of the CMS detector. Figure from Ref. [49].

The coordinate system in CMS has its origin centered at the nominal collision point within the detector. The z-axis follows the beam line, the y-axis points vertically upward, and the x-axis points radially inward toward the center of the LHC ring. The azimuthal angle ϕ is measured from the x-axis in the $x - y$ plane, with the radial coordinate denoted as r, and the polar angle θ is measured from the z-axis. However, θ is not often used because it is not Lorentz invariant for boosts along the direction of the beam. Instead, the pseudorapidity is defined as $\eta = -\ln\left(\tan\frac{\theta}{2}\right)$, which is Lorentz invariant. From this, it is possible to define the momentum orthogonal to the beam direction, denoted as p_T. It is also worth defining the notion of angular distance between two directions as $\Delta R = \sqrt{(\Delta\phi)^2 + (\Delta\eta)^2} = \sqrt{(\phi_1 - \phi_2)^2 + (\eta_1 - \eta_2)^2}$, which will be useful throughout the analysis.

The silicon tracker is designed to measure the trajectory, charge and momentum of charged particles traversing it, as well as to reconstruct secondary vertices. It comprises two types of silicon detectors: the pixel detector (inner tracker) and the silicon strip tracker (outer tracker). They operate by measuring the ionization of charged particles. When a charged particle traverses the doped silicon wafer, it creates electron-hole pairs that move toward collection electrodes due to an applied electric field. These pairs are organized into silicon strips or pixels,

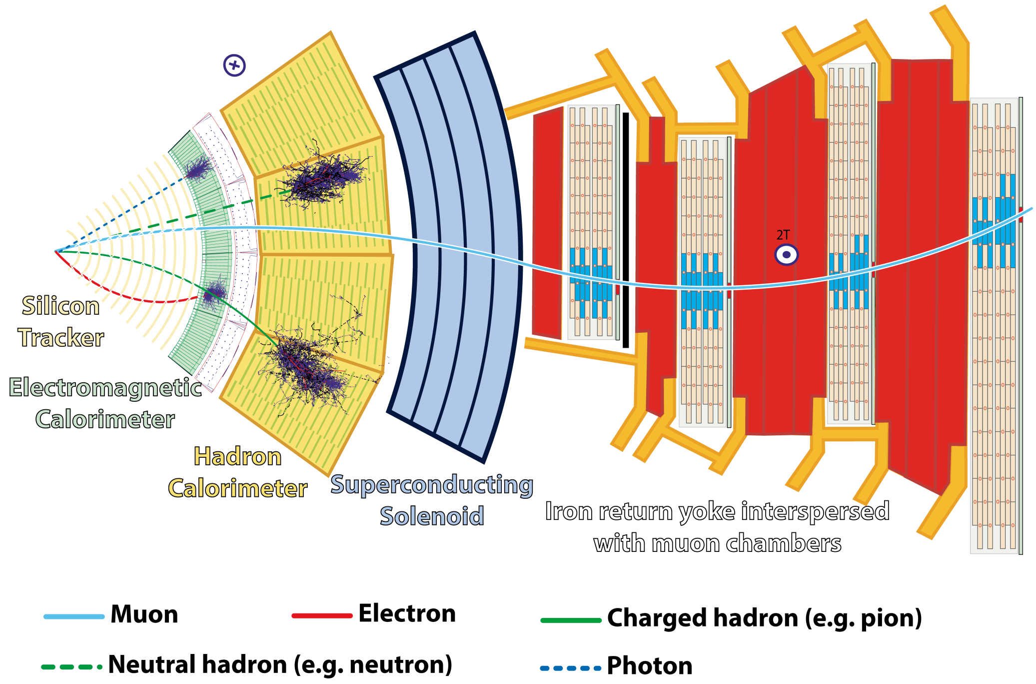

Figure 11: A slice of the CMS detector, with an illustration of the behaviour of different particles. Figure from Ref. [50].

providing a two-dimensional measurement. Multiple silicon wafers are arranged in different layers, and the hits measured in each layer are used to reconstruct the tracks of charged particles through the detector. The pixel detector is the innermost component, consisting of four barrel layers and three endcap disks. The silicon strip tracker is positioned just outside, extending to a radius of 1.1 m and comprising 15148 strips arranged in ten barrel layers and twelve endcap disks.

The primary purpose of the electronic calorimiter (ECAL) is to measure the energy and direction of electrons, positrons and photons. It is constructed with homogeneous lead tungstate ($PbWO_4$) crystals that serve as both active scintillating material to detect the electromagnetic signal and absorbing material to initiate electromagnetic (EM) showers. Energy deposition is measured through crystal ionization, and their deexcitation photons are detected by dedicated photodetectors. The short radiation length of the crystals, $X_0 = 0.89$ cm, ensures that the EM showers remain confined within a small region. The photodetectors are designed to withstand the high radiation and high magnetic field environment while being sufficiently fast compared to the LHC bunch crossing time. The ECAL consists of main parts: the ECAL barrel (EB), covering $|\eta| < 1.479$, composed of 61200 crystals and which uses avalanche photodiodes, and the ECAL endcaps (EE), covering $1.479 < |\eta| < 3.0$, composed of 7324 crystals in each (lower granularity compared to the barrel) and which use vacuum phototriodes. To account for the reduced endcap granularity, preshower detectors are installed before the lead tungstate crystals, covering $1.653 < |\eta| < 2.6$, intended for identifying neutral pions, distinguish electrons against minimum ionizing particles, and improve position measurements. This design enables the ECAL to completely stop electrons and photons emerging from the tracker, allowing for accurate energy measurement.

Four hadronic calorimeters (HCAL) are positioned outside the ECAL. They are designed to generate hadronic showers when strongly interacting particles pass through their absorption material. These particles interact in the absorber layers, producing numerous secondary particles and often showers, which are measured by the scintillators. The HCAL are bigger than the ECAL because the nuclear interaction length λ_{int} is also larger than the electromagnetic radiation length X_0 (e.g., for iron, $\lambda_{\text{int}} = 16.8$ cm, while $X_0 = 1.76$ cm [51]). The HCAL barrel (HB) rests between the ECAL and the magnet ($R = 1.77 - 2.95$ m), covering $|\eta| < 1.4$. The HCAL endcap (HE) covers $1.3 < |\eta| < 3.0$. Both the HB and the HE are made of brass and plastic scintillators. The HCAL outer detector (HO) is placed outside the magnet in the barrel region ($|\eta| < 1.26$) to catch the tail of the shower, and it is made of iron and plastic scintillators. To ensure optimal efficiency in different pseudorapidity ranges, there is a fourth HCAL placed in the endcap regions after the muon systems. The HCAL forward detector (HF) covers $3.0 < |\eta| < 5.0$ at $|z| = 11.2$ m, where it is subject to much higher radiation. It is distinguished from the other HCAL sections because it is built with steel and quartz fibers, leading to shorter hadronic showers for better absorption of very forward hadron showers. Note that the ECAL already absorbs a fraction of the energy of the hadrons, but the HCAL design allows it to fully stop the hadrons and measure any remaining energy, which is later combined with the ECAL information to obtain a complete picture.

Muon identification was a focal point for CMS because muons produced in proton-proton collisions offer clear lepton signatures for a wide range of physics processes and helps with their reconstruction. The CMS muon system consists of several subdetectors dedicated to measure muons with high precision. To achieve accurate muon identification, the muon detectors were designed with extensive pseudorapidity coverage, up to $\eta = 2.4$. CMS's muon system uses three types of detectors: Drift Tubes, Resistive Plate Chambers and Cathode Strip Chambers. Muon Drift Tubes (DT) contain a wire and a gas mixture (85% Ar, 15% CO_2) at atmospheric pressure that ionizes when traversed by a muon. The deexcitation electrons follow the electric field to reach the wire, recording the signal. By recording the distance from the wires and the location along the wires, the DTs determine two coordinates of the muon's positions. Resistive Plate Chambers (RPC) are gaseous (95.2% $C_2H_2F_4$, 4.5% i-C_4H_{10}, 0.3% SF_6) parallel plate capacitors with high timing resolution. Cathode Strip Chambers (CSC) consist of positively charged anode wires crossed with negatively charged cathode panels within a gas volume (40% Ar, 50% CO_2, and 10% CF_4), which ionize when traversed by a muon: positive ions move toward the cathode and the electrons move toward the anode wires. In the CMS detector's barrel ($|\eta| < 1.2$), the DTs are arranged in four concentric layers interleaved with five layers of the iron magnet yoke and six layers of RPCs, as shown in Figure 11. In the endcap region, reaching $\eta = 2.4$, there are three RPC layers (up to $\eta = 1.6$) and six CSC layers, chosen in this region for their ability to resist high non-uniform magnetic fields. Muons do not deposit much energy in matter, so they pass through both calorimeters with most of their momentum. The muon chambers then provide further information about the muon's trajectory, as they are the only particles with a clear signal in this section. These trajectories, combined with those of the trackers, allow for better muon identification and provide additional data on their momenta.

Storing all recorded events in the detector is impractical, so only events meeting specific conditions are preserved. The Level 1 (L1) Trigger uses local trigger information from all subdetectors, excluding the Inner Tracker, to determine whether to save an event. With the aid of custom hardware and firmware, it reduces the event rate from 40 MHz to 100 kHz. It considers information from the four highest E_T electrons, photons, central jets, forward jets, tau-jets, the four highest p_T muons, the event's missing transverse energy (MET), and the scalar sum of the jet transverse momenta (HT). Subsequently, data is processed by the High-Level Trigger (HLT), a comparatively slower software, to further filter events based on trigger menus, reducing the rate to around 1 kHz. The CMS offline physics object reconstruction is achieved using the Particle Flow (PF) algorithm, which integrates information from all subdetectors to reconstruct all particles in the event.

The Compact Muon Solenoid experiment is one of the largest international scientific collaborations in history, involving more than 6000 particle physicists, engineers, technicians, students and support staff from 257 institutes in 59 countries as of October 2023 [52].

2.3 The discovery of the Higgs boson

Nearly 50 years after the Higgs boson had been proposed, in 2012, the CMS and ATLAS collaborations observed a new scalar boson with a mass of 125 GeV [7, 8]. The properties of this particle were compatible with those of the Higgs boson, including its spin and mass (in 2012 precision electroweak measurements and direct searches at LEP had constrained the mass of the Higgs boson to be in the interval 114.4 GeV $< m_H <$ 152 GeV at 95% confidence level (CL) [53, 54]).

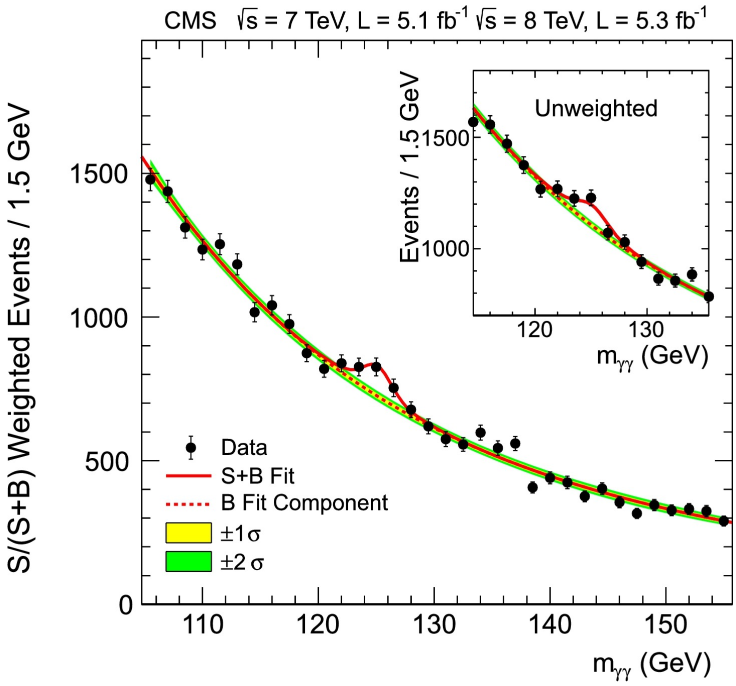

Figure 12: The diphoton invariant mass distribution computed by CMS from Ref. [7]. The lines represent the fitted background and signal, and the coloured bands $\pm 1\ \sigma$ and $\pm 2\ \sigma$ in the background estimate.

The CMS experiment used data recorded at $\sqrt{s} = 7$ and 8 TeV, with integrated luminosities of up to 5.1 fb^{-1} at 7 TeV and 5.3 fb^{-1} at 8 TeV. For the search, five decay modes were employed: H $\rightarrow \gamma\gamma$, ZZ^*, WW^*, $\tau^+\tau^-$ and $b\bar{b}$, which according to the SM is about 89% of all the decay modes of the Higgs boson (see Table 3). They reported an excess of events over the expected background, consistent with the production of a new particle with mass near 125 GeV, with an observed local signigicance of 5.0 standard deviations (σ). The strongest evidence came from the two final states with the best mass resolution, which are $H \to \gamma\gamma$ with a significance of 4.1σ and $H \to ZZ^*$ with a significance of 3.2σ. Moreover, $H \to \gamma\gamma$ indicated that the new particle was a boson with spin different from one [7]. Figure 12 presents the diphoton invariant mass $m_{\gamma\gamma}$ presented by CMS in 2012, where the excess at 125 GeV is evident in the weighted and unweighted distributions.

The confidence level of the combined result as a function of the Higgs boson mass is presented in Figure 13. The observed values are shown as the solid points, while the dashed line represents the median of the expected results for the background-only hypothesis. The green and yellow bands indicate the ranges where CLs values are expected to lie in 68% and 95% of the experiments under the background-only hypothesis. The red horizontal lines indicate CLs values of 0.05, 0.01, and 0.001. The mass regions where the observed CLs values are below these lines are excluded with the corresponding (1 - CLs) confidence levels. In the range $121.5 < m_H < 128$ GeV a significant excess is observed, and the SM Higgs boson cannot be excluded at 95% CL. They also determined the Higgs boson mass by using the $\gamma\gamma$ and ZZ^* decay modes, obtaining a value of $m_H = 125.3 \pm 0.4$ (stat.) $\pm$ 0.5 (syst.) GeV $= 125.3 \pm 0.6$ GeV.

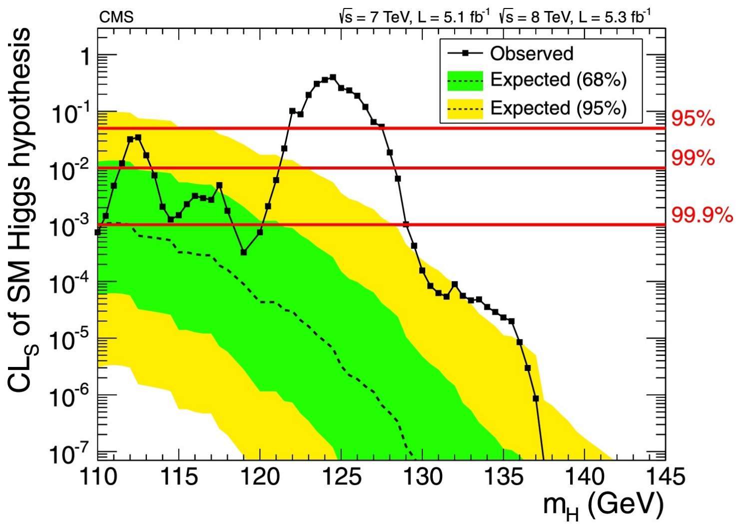

Figure 13: The CLs values for the SM Higgs boson hypothesis as a function of the Higgs boson mass in the range 110-145 GeV, by CMS from Ref. [7].

In ATLAS analysis [8], they reported a significance of 5.9σ and a mass of $m_H = 126.0 \pm 0.4$ (stat.) $\pm$ 0.4 (syst.) GeV $= 126.0 \pm 0.6$ GeV, compatible with CMS's results.

Chapter 3

Analysis

This chapter constitutes the core of this dissertation. Here, we will discuss the analysis conducted, starting with a general overview, followed by an explanation of the samples, triggers, and object definitions. We will then talk about the corrections applied to the data and simulations to enhance the analysis results. Additionally, we will cover the criteria used in event selection and how the signal and background have been modeled. Finally, we will present the expected upper limits of the branching ratio for each channel, as this analysis will only be working with simulated signal, alongside simulated and real background data. The chapter concludes by addressing the subsequent steps required before data unblinding and the attainment of the final experimental measurement, as well as suggesting other ideas to improve the results.

3.1 Analysis overview

This analysis uses data from proton-proton collisions corresponding to an integrated luminosity of 39.54 fb^{-1} at $\sqrt{s}$ =13 TeV, collected by the CMS detector at LHC in 2018 during Run 2. It only targets the Higgs boson production mode via gluon fusion (ggH), which accounts for approximately 87% of the Higgs boson production at LHC at $\sqrt{s}$ =13 TeV. Although it is possible to extend this analysis to include more production modes, time constraints have led us to focus to the main production channel. The final states of interest consist of an isolated and energetic photon, a charged meson pair, and photons compatible with a third (and sometimes fourth) neutral meson, with 0 hadronic jets and no additional leptons (e/μ). The mesons considered here are a ϕ, a ω and a D^{*0}, each further decaying into two charged particles and a third (and fourth) neutral one (see Table 6).

$$
\begin{array}{ll}
\mathrm{H} \rightarrow \phi\gamma\ , & \phi \rightarrow \pi^+\pi^-\pi^0 \\
\mathrm{H} \rightarrow \omega\gamma\ , & \omega \rightarrow \pi^+\pi^-\pi^0 \\
\mathrm{H} \rightarrow D^{*0}\gamma\ , & D^{*0} \rightarrow D^0\pi^0/\gamma,\ D^0 \rightarrow K^{\mp}\pi^{\pm} \\
\mathrm{H} \rightarrow D^{*0}\gamma\ , & D^{*0} \rightarrow D^0\pi^0/\gamma,\ D^0 \rightarrow K^{\mp}\pi^{\pm}\pi^0
\end{array}
$$

Table 6: Higgs rare decays under study in this analysis.

The analysis strategy involves categorizing events to increase the signal to background ratio. In our production mode (ggH), the largest background source in this analysis consists of γ plus jets events.

The branching fractions of rare Higgs boson decays to a meson and photon can be computed using a factorization approach in QCD. The calculation considers both direct and indirect contributions, as explained in the first chapter and depicted in Figure 6. The interference between these components is significant. In the SM, the indirect component dominates, and the Higgs boson couplings to light quarks are probed by searching for modifications in this branching fraction due to interference effects.

As previously explained, given the exotic nature of the decays under study, the theoretical decay widths being so small, the large hadronic background at the LHC, and the limited amount of data collected, we cannot aim for precise measurements of the branching fractions. Instead, the end goal of this thesis is to calculate a reasonable upper limit on the branching ratio of the aforementioned Higgs boson decays, using Monte Carlo (MC) samples to model the SM expected signal. To obtain a competitive, real result, this initial estimation requires further refinement and improvement, such as considering additional background sources, systematic uncertainties, etc.

The main difference between this analysis and the study of the three decays in the upper half of Table 4 is that, in contrast to those, we are studying 3-body decays with neutral particles, which are more challenging to track than charged ones. The framework used for this analysis builds upon the existing framework for the simpler two-body decays currently under analysis by the Particle Physics Collaboration at MIT. To extend their study to include three-body decays involving neutral particles, our main focus has been on accurately recovering the missing neutral particles.

3.2 Samples and triggers

To develop this analysis, the data file format used is one designed by CMS, which is an extended version of `NANOAOD`. It is based on the official `NANOAODv9` recipe and includes the reconstructed mesons, as described in Section 3.3, as additional objects. The `NANOAOD` format consists of an Ntuple-like structure used by CMS, which can be read using bare root, and containing the per-event information that is needed in most generic analyses [55]. This analysis is performed using the `ROOT` data analysis framework, an open-source data analysis tool commonly used in high energy physics written mainly in C++ [56].

3.2.1 Data and Tau trigger

Events are selected from proton-proton collision data at a center-of-mass energy of $\sqrt{s}$ =13 TeV and a bunch spacing of 25 ns, collected by the CMS experiment during the LHC's Run 2 in 2018, corresponding to a total integrated luminosity of 39.54 fb^{-1}. Good run ranges and luminosity blocks are chosen based on criteria encoded in a golden JSON file.

To filter data in the gluon fusion production mode, a tau-like trigger is employed. This Tau trigger selects a photon with $p_T^{\gamma} > 35$ GeV and a ditrack system with $p_T^{\text{jet}} > 35$ GeV, after going through the L1 trigger, which also imposes rapidity restrictions of $|\eta^{\gamma}| < 2.1$ and $|\eta^{\text{jet}}| < 2.1$. The trigger is applied to both data and MC. Introduced in 2018, this trigger recorded events enriched in gluon fusion production of the Higgs boson and VBF that were not registered by the dedicated trigger, providing an effective luminosity of 39.54 fb^{-1}. The trigger selecting events during 2018 is encoded as `Photon35_TwoProngs35`. **[TODO:** Should I include trigger efficiencies for each channel in the appendix? If so, how do I obtain these plots?] The datasets used in gluon fusion and VBF analysis are detailed in Table 7.

Year	Dataset	Integrated luminosity [fb^{-1}]
2018	`/Tau/Run2018B-UL2018`	0.67
2018	`/Tau/Run2018C-UL2018`	6.94
2018	`/Tau/Run2018D-UL2018`	31.93

Table 7: Datasets used in the gluon fusion analysis from the campaign MiniAODv2 of the MINIAOD data tier.

3.2.2 Background simulation

The background estimation will ultimately rely solely on data. However, at the early stage of this analysis, simulated samples are used to understand the background processes affecting the different selected final states. The main background process for the gluon fusion production mode is a single photon and jets.

Every event is generated at leading order (LO) precision using the MADGRAPH5 generator `MG5_aMC@NLO` [57] and POWHEG [58], while PYTHIA8 [59] is used for the hadronization. For all simulations, the NNPDF 3.1 [60] next-to-next-to-leading-order (NNLO) parton distribution functions (PDFs) are used, while the modeling of the underlying event is generated using the CMS Pythia 5 (CP5) tunes [61]. The Run 2 legacy reconstruction algorithms [62] are used for all the MC and data samples. The campaign and global tag used to produce the background and signal MC samples are `RunIISummer20UL18MiniAODv2-106X` and `upgrade2018_realistic_v16_L1v1`, respectively. Table 8 summarizes the list of datasets used for the study along with their cross sections [63].

Monte Carlo name	Cross section [pb]
`GJets_HT-40To100_TuneCP5_13TeV-madgraphMLM-pythia8`	18540 (LO) $\times$ 1.26
`GJets_HT-100To200_TuneCP5_13TeV-madgraphMLM-pythia8`	8644 (LO) $\times$ 1.26
`GJets_HT-200To400_TuneCP5_13TeV-madgraphMLM-pythia8`	2183 (LO) $\times$ 1.26
`GJets_HT-400To600_TuneCP5_13TeV-madgraphMLM-pythia8`	260.2 (LO) $\times$ 1.26
`GJets_HT-600ToInf_TuneCP5_13TeV-madgraphMLM-pythia8`	86.58 (LO) $\times$ 1.26

Table 8: MC samples used for the gluon fusion production mode. The normalization of γ+jets is scaled by 1.26 [64] **[TODO:** WHY?].

3.2.3 Signal simulation

The only Higgs boson production mode studied, gluon fusion, is generated at next-to-leading order (NLO) using the POWHEGv2 event generator extended with the MiNLO procedure [65]. The production rates and kinematic distributions for the Higgs boson with $m_H = 125$ GeV are assumed throughout. In particular, the cross section for gluon fusion is computed at NNLO in QCD and NLO in electroweak accuracy, resulting in 48.58 pb, as provided by the LHC Higgs Cross Section Working Group in Ref. [10].

The decay of the Higgs boson is handled by Pythia. Direct and indirect effective vertices are not simulated. The expected SM branching fractions of the Higgs rare decays are as previously shown in Table 5: $\mathcal{B}(\mathrm{H} \to \phi\gamma) = (2.31 \pm 0.11) \times 10^{-6}$ and $\mathcal{B}(\mathrm{H} \to \omega\gamma) = (1.48 \pm 0.08) \times 10^{-6}$, while $\mathcal{B}(\mathrm{H} \to D^{*0}\gamma)$ has not yet been computed. In the analysis, however, the branching ratios are set to

$$\mathcal{B}(\mathrm{H} \to \phi\gamma) = \mathcal{B}(\mathrm{H} \to \omega\gamma) = \mathcal{B}(\mathrm{H} \to D^{*0}\gamma) = 1\,,$$

because **[TODO:** explain why**]**. The branching fractions of the meson decays used are also shown in Table 4, but further detailed in Table 9.

Meson decay channel	SM $\mathcal{B}$ (%)
$\phi \to \pi^+\pi^-\pi^0$	15.4 ± 0.4
$\omega \to \pi^+\pi^-\pi^0$	89.2 ± 0.7
$D^{*0} \to D^0\pi^0$	64.7 ± 0.9
$D^{*0} \to D^0\gamma$	35.3 ± 0.9
$D^0 \to K^\mp\pi^\pm$	3.962 ± 0.031
$D^0 \to K^\mp\pi^\pm\pi^0$	14.43 ± 0.50

Table 9: Meson decay branching ratios used throughout the analysis, from the PDG [11].

3.3 Object definitions

This analysis primarily relies on photons and charged tracks to extract the final state signature of exclusive hadronic decays, while also making use of other physics objects such as additional leptons (or the lack thereof) and hadronic jets to suppress background. All used objects, except the mesons, are discussed in this section, with the next section dedicated solely to meson reconstruction.

Primary vertex (PV): To consider an event, it must contain at least one primary vertex, which is regarded as the vertex of the hard interaction. There should be a minimum of four tracks associated with the selected primary vertex (from the Higgs boson, the photon and the ditrack system). For events with multiple selected vertices, the PV is chosen to be the vertex corresponding to the hardest scattering in the event, determined using tracking information alone, as described in Ref. [66].

Jets: During the reconstruction of a proton-proton (pp) collision, jets are often reconstructed with a p_T that differs from that of the final-state particles within the jet. The jet energy corrections (JEC) adjust the reconstructed jet energy to match the true energy of the final-state particles. The CMS collaboration has developed a factorized approach to these JEC, consisting of multiple levels that correct various physics or detector effects. This approach provides flexibility in the corrections to suit various types of analyses. These correction levels are commonly referred to as L1FastJet, L2Relative, L3Absolute, and L2L3Residual.

The flow of these JEC is as follows: Jets are reconstructed from particle flow (PF) candidates using the anti-k_T clustering algorithm with a distance parameter of $R = 0.4$ as implemented by FastJet [67]. Jets within this small cone (referred to as AK4 jets for $R = 0.4$) are selected among those with $p_T > 25$ GeV and $|\eta| < 4.7$ for forward tagging. At the LHC, a significant number of pp collisions occur simultaniously during one bunch crossing, with soft ones contaminating the collision of interest. To mitigate this effect, known as *pileup* (PU), charged hadrons not originating from the primary vertex are removed using the charged hadron subtraction (CHS) algorithm [68, 69]. The tight pileup ID criterion is applied to reduce the contamination of jets with $p_T < 50$ GeV initiated by the pileup interactions. Jets are corrected for the response inside the detector, differentially in $|\eta| - |\phi|$, for the pileup contributions, and for data only, the residual difference observed between data and simulation.

In the current analysis version, the `Summer19UL` jet energy corrections set is used, as well as the DeepJet tagging algorithm with the medium working point to identify b-jets [70].

Missing energy: The p_T^{miss} measures the transverse momentum imbalance in the event. To estimate it, the deepMET algorithm [71] is used, and p_T^{miss} filters are then applied to account for instrumental noise in the detector and minimize the impact of the non-collisional background.

Photons: Photon candidates are reconstructed as SuperCluster objects in the ECAL with $E_T > 38$ GeV and $|\eta^\gamma| < 2.1$ in both the barrel and endcap regions. In addition, photons have to satisfy the multivariate analysis (MVA) based selection identification (mvaID) criteria following the `Fall17IsoV2` recipe [72]. For the production mode used, the mvaID provides 80% (90%) signal selection efficiency for the endcap (barrel) region. The mvaID criteria include photon isolation, charged hadron isolation, and require photons to pass shower shape preselection cuts [73]. The photon's ECAL cluster must be inconsistent with charged particle tracks reconstructed in the silicon tracker to reject electrons faking photons, achieved using a conversion safe electron veto. Residual E_T -dependent photon energy scale and smearing corrections are applied. Additional photons with looser requirements ($E_T > 20$ GeV and the WP90 version of the photonID) are also vetoed to reduce the potential contribution of diphotons. Table 10 summarizes the criteria for photon selection.

Selection criteria (γ from PV)	
p_T^γ	> 38 GeV
$\|\eta^\gamma\|$	< 2.1
mvaID	WP90/WP80
electron Veto	Yes

Table 10: Selection criteria applied to the photon from the primary vertex.

An additional correction was attempted, involving shifting the photon's origin to that of the PV of the meson. This slight adjustment to the initial coordinates led to a minor change in the four-momentum variables of the photon, but it did not consistently reduce the discrepancy with the generation-level particle values. Consequently, it was discarded and not used.

3.4 Meson reconstruction [TODO: ADD FOURTH D0* CHANNEL]

The ϕ, ω and D^{*0} mesons decay products are reconstructed using charged particle tracks measured in the tracker, as well as energy deposited in the ECAL compatible with neutral particles coming also from the PV. For the ϕ and ω mesons, the targeted charged ditrack is $\pi^{\pm}\pi^{\mp}$, while for the D^{*0} meson the charged ditrack is $K^{\mp}\pi^{\pm}$.

In the following sections, the term *ditrack system* will refer to the system of the two charged tracks, and even though they not form a real particle, notions like ditrack mass will be used (understand the mass of the ditrack as the mass component of the sum of the four-momenta of both tracks). To refer to the meson originating from the PV, namely ϕ, ω and D^{*0}, terms like *meson* or *full meson* will be used, emphasizing that the neutral particles have been accounted for. Some considerations have been made to precisely reconstruct the full meson:

Track selection: To be selected, the tracks need to satisfy a "high purity" reconstruction criteria, which considers the number of tracker layers with hits, track fit quality, and the impact parameter values relative to their uncertainties. For a detailed description of the algorithm, refer to Ref. [74].

Meson decay vertex: The meson decay vertex is determined using the standard CMSSW [75] kinematic vertex fitting package, as described in Ref. [76]. Using the candidate's decay vertex and its associated momentum, a newly fitted transient track is constructed to represent the meson candidate. Then, for each primary vertex, the track is extrapolated to the nearest point in 3D space. The meson vertex's longitudinal distance is required to be within 24 cm from the center of the detector.

Isolation: To ensure good track selection, a dedicated isolation criterion of the candidate based on the tracks is used. This dimensionless isolation parameter (Iso) is determined from the meson's momentum and other tracks within a cone of radius $\Delta R = 0.3$ around the ditrack system's direction. Only tracks with $p_{\mathrm{T}} > 0.9$ GeV associated with the same meson vertex are considered, excluding the charged-hadron candidates that define the ditrack. The definition is as follows:

$$\mathrm{Iso} = \frac{p_{\mathrm{T}}^{\mathrm{meson}}}{p_{\mathrm{T}}^{\mathrm{meson}} + \sum_{\mathrm{trk}} |p_{\mathrm{T}}^{\mathrm{trk}}|}$$

A high isolation value will be required to consider a meson candidate (over 0.9).

Neutral particle photons: For each selected ditrack, up to two photons with $p_{\mathrm{T}} > 5$ GeV are recovered in a small cone of $\Delta R = 0.05$ around the ditrack direction. These photons account for the recovery of neutral particles, as $\pi^0 \to \gamma\gamma$ in $\sim 98.8\%$ with $c\tau = 25$ nm [11]. From generation-level MC we know that photons coming from neutral particle decays that in turn come from the three-body decays must be very collimated with the ditrack system. In the case of the ϕ/ω channels and the D^{*0} channel when D^0 decays into three bodies, these photons directly originate from the π^0 of the three-body decay. In the case of the D^{*0} channel, the photon comes either directly from $D^{*0} \to D^0\gamma$ or from de decay of the π^0 from $D^{*0} \to D^0\pi^0$.

Ditrack mass hypothesis: The invariant mass of the refitted ditrack system is also used to reduce contamination from background events. The mass of the pair, assuming the charged-pion hypothesis for the two tracks, is consistent with the charged components of the ϕ

and ω mesons. Since the ditrack system is not a real resonance, its mass is very wide but consistent and useful for reducing background events. In the case of the D^{*0} channel, two scenarios are considered. On the one hand, when D^0 decays into a pair of charged particles (kaon-pion) the ditrack system's invariant mass is a real narrow resonance (namely D^0) coherent with the mass of that meson. On the other hand, when D^0 decays into a pair of charged particles and a neutral pion, one finds the same scenario as for the ϕ/ω decay channels.

The exact used selection criteria will be presented at the end of this section, but it is worth noting that for the ϕ/ω three-body decays involving a π^0, the mass of the ditrack is approximately two-thirds of the full meson's mass (each pion carries roughly a third of the energy).

Furthermore, instead of recovering the ditrack invariant mass by only retrieving the mass component of the sum of both four-momenta, the CMSSW kinematic fit has been employed. To study the performance of this fit, it is useful to define the *residual* as the difference between the reconstructed values and the corresponding generation-level ones. Figure 14 displays the residual of the ditrack invariant mass reconstruction with and without the kinematic fits with vertex constraint for every decay mode. Table 11 shows the

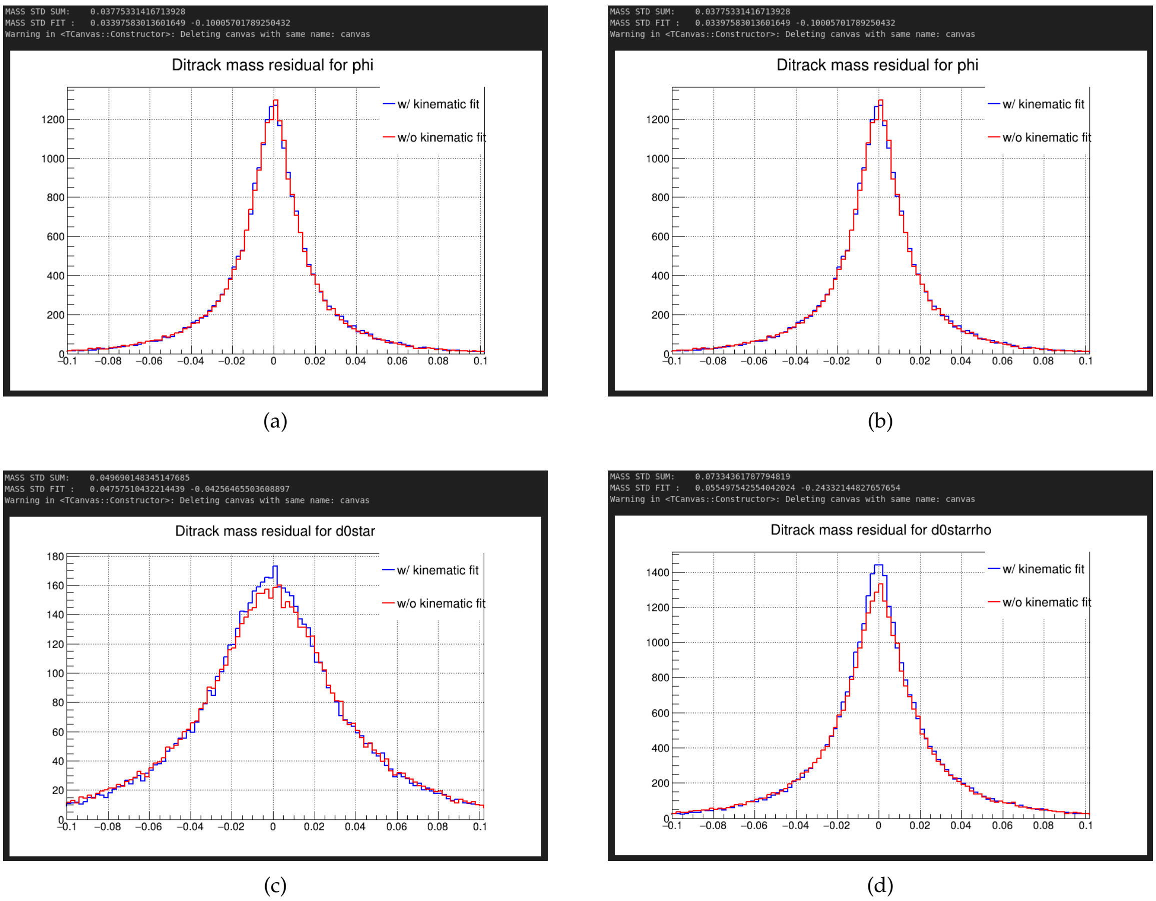

Figure 14: Ditrack mass residuals for the different decay channels. (a) is for ϕ, (b) is for ω, (c) is for D^{*0} 2-body and (d) is for D^{*0} 3-body.

mean squared errors with respect to generation-level, both with and without the kinematic fit for each channel. Applying the kinematic fit improves the reconstructed ditrack invariant mass values for all channels.

Decay channel	MSE without kinematic fit	MSE with kinematic fit
ϕ	37.8 MeV	34.0 MeV (-10%)
ω	?? MeV	.?? MeV (-x%)
D^{*0} 2-body	49.7 MeV	47.6 MeV (-4%)
D^{*0} 3-body	73.3 MeV	55.5 MeV (-24%)

Table 11: Mean squared errors (MSE) with and without the kinematic fit for each decay mode.

Meson mass hypothesis: The simplest way to reconstruct the four-momentum of the full meson is by summing the four-momenta of the ditrack system and those from the photons compatible with the decay of neutral particles. This approach was initially used for all channels. Nevertheless, for the ϕ, ω and D^{*0} 3-body decay channels, additional corrections were applied.

Consider that the photons in the ΔR cone come from the $\pi^0 \to \gamma\gamma$ decay. When only one photon is recovered, it means that either both photons ended up in the same ECAL crystal, or that one of them was too soft to be measured ($p_T < 5$ GeV) and therefore only one is detected. Following the first hypothesis, we can interpret the energy deposited in the same ECAL cell as the energy from the full pion. To account for this, whenever only one photon is recovered, we assign this object a non-zero mass (the pion's mass) before adding the four-momenta. This correction is of very low energy, and thus the changes in p_T, η or ϕ of the full meson are imperceptible, but its mass is visibly affected. Figure 15 and Table 12 show the residual of the full meson invariant mass reconstruction and the MSE, respectively, with and without the π^0 mass correction for the ϕ and ω decay modes.

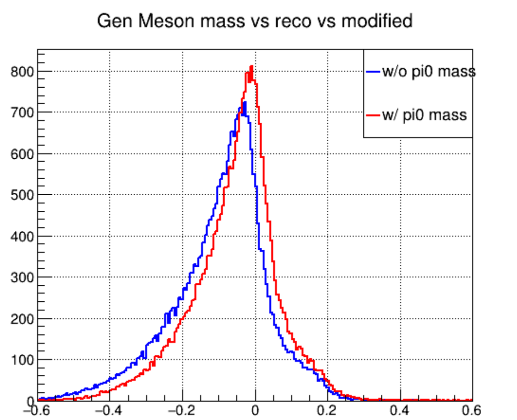

(a)

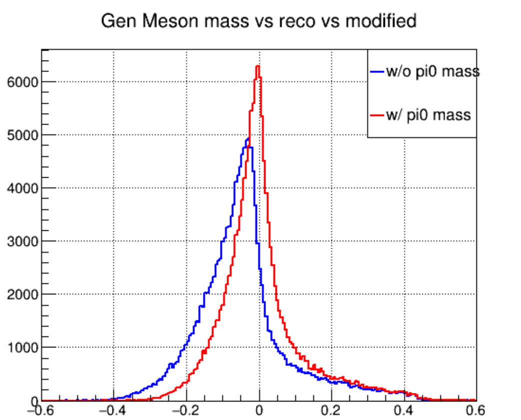

(b)

Figure 15: Full meson mass residuals for the different decay channels. (a) is for ϕ, (b) is for ω.

This slight improvement will enable us to narrow some selection cuts and reduce more background events, ultimately improving the final result.

[TODO: IDEA: force always mass of the pi0 at the sum of the recovered photons

Decay channel	MSE without m_{π^0} correction	MSE with m_{π^0} correction	
ϕ	130.2 MeV	117.7 MeV	(-10%)
ω	127.9 MeV	113.1 MeV	(-12%)

Table 12: Mean squared errors (MSE) with and without the m_{π^0} correction for the ϕ and ω decay modes.

(aka pi0). Make the E, eta and phi the same, but by forcing pi0's mass change a bit pT. Then add the neutral to the ditrack to compare all variables with the recovered ones and the gen level full mesons.]

Meson transverse momentum correction: To compute the upper limits of the branching ratios of the decays, the Higgs boson invariant mass is going to be calculated. To achieve an accurate value, it is crucial that the two objects involved, namely the photon and the full meson, are recovered with the utmost precision. The accuracy of the Higgs boson invariant mass mainly relies on the accuracy of the transverse momenta of both particles involved. The other five variables (η and ϕ of both particles and the mass of the full meson) are either already well measured or, in the case of the mass, too low in energy to significantly impact the computation. Improving the transverse momentum of the photon is very challenging, as it already undergoes the reconstruction algorithm briefly discussed in the previous section. Therefore, the main emphasis should be on recovering the p_T of the full meson as precisely as possible.

In each decay channel, the ditrack system variables are measured with remarkable accuracy. Figure X displays the residuals of the ditrack transverse momentum, mass, η and ϕ with respect to their generation-level MC value for every decay mode. All histograms are normalized to the same area for comparing the various channels.

[TODO: Include residuals]

[TODO: comment on errors of variables]

The initial approach to reconstruct the full meson's transverse momentum is to sum the four-momenta of the ditrack system and those from the photons compatible with the decay of neutral particles. The main source of discrepancy between the full meson's transverse momenta and their generation-level MC values arises from the poorly reconstructed neutral particles. Given that the pions decay into softer photons that are hard to recover, many events exhibit missing energy, resulting in the full meson's p_T being generally less energetic than expected. Figure X shows the residuals of the full meson's transverse momentum with respect to their generation-level MC value for each decay mode.

[TODO: Include residuals]

[TODO: comment plot]

To address this issue, dedicated Boosted Decision Trees (BDTs) have been implemented for each channel using the Toolkit for Multivariate Data Analysis for root, also known as `TMVA` [77]. This machine learning (ML) technique will correct for the full meson's p_T. A boosted decision tree (BDT) is a ML classifier or regressor algorithm based on a flowchart-like structure in which each internal node represents a test on an attribute, each branch signifies the test's outcome, and each leaf node denotes a class level. For more detailed information, refer to Refs. [77, 78].

[TODO: Three different variable categories: dimensionless, dimensionfull and normalized. Many iterations performed. Present the models, and attatch hyperparameters in the appendix. For each channel show pt generation, reco and corrected + residuals corrected and reco. Present table with MSE improvements.]

[TODO: Talk about importance of not biasing the result, not including certain variables and why a scale factor is predicted instead. Introduction of "background shaping function" to control for biasing.]

Tables 13 and 14 summarize the meson candidate selection criteria used.

Variable	$\phi(\pi^{\pm}\pi^{\mp}\pi^{0})$	$\omega(\pi^{\pm}\pi^{\mp}\pi^{0})$
Meson mass	0.96 ± 0.26 GeV	0.785 ± 0.215 GeV
Ditrack mass	0.59 ± 0.25 GeV	0.47 ± 0.15 GeV
$p_{\mathrm{T}}^{\mathrm{diTrk}}$	> 10 GeV	> 15 GeV
$p_{\mathrm{T}}^{\mathrm{leadTrk}}$	> 5 GeV	> 8 GeV
$\#\gamma^{\mathrm{diTrk}}$	> 0	> 0
$\Delta(\phi^{\mathrm{diTrk}}, \phi^{\gamma_{\mathrm{H}}})$	$\pi \pm 2.3$	$\pi \pm 2.3$
$\Delta(\eta^{\mathrm{diTrk}}, \eta^{\gamma_{\mathrm{H}}})$	0 ± 1.9	0 ± 1.9
Iso	> 0.95	> 0.95

Table 13: Selection criteria applied to the ϕ and ω mesons used in the analysis.

Variable	$D^{*0}(K^{\mp}\pi^{\pm}(\pi^{0}/\gamma))$	$D^{*0}(K^{\mp}\pi^{\pm}\pi^{0}(\pi^{0}/\gamma))$
Meson mass		$x.xx \pm x.xx$ GeV
Ditrack mass	1.865 ± 0.060 GeV	$x.xx \pm x.xx$ GeV
$p_{\mathrm{T}}^{\mathrm{diTrk}}$	> 40 GeV	$> xx$ GeV
$p_{\mathrm{T}}^{\mathrm{leadTrk}}$	> 21 GeV	$> xx$ GeV
$\#\gamma^{\mathrm{diTrk}}$		$> xx$
$\Delta(\phi^{\mathrm{diTrk}}, \phi^{\gamma_{\mathrm{H}}})$	$\pi \pm 2.3$	$\pi \pm 2.3$
$\Delta(\eta^{\mathrm{diTrk}}, \eta^{\gamma_{\mathrm{H}}})$	0 ± 1.9	0 ± 1.9
Iso	> 0.91	$> xx$

Table 14: Selection criteria applied to each channel of the D^{*0} meson decay used in the analysis.

[TODO: Talk about the criteria used a bit]

3.5 Event selection

[TODO: Gluon fusion selection for each channel]

[TODO: Explain we only pick one goodphoton/goodmeson for each event, and criteria]

3.6 Signal and background modelling

[**TODO:** signal, background model from MC and data, bias studies]

3.7 Results

[**TODO:** Present results]

3.8 Future potential improvements

[**TODO:** talk about MVA, data-MC corrections, and what are next steps before unblinding data]

Conclusions

These are the conclusions of the project.

Appendix A

Appendix

First appendix

References

[1] D.H. Perkins, "*Introduction to High Energy Physics*", Addison-Wesley, Reading, USA (1982).

[2] M.E. Peskin and D.V. Schroeder, "*An Introduction to Quantum Field Theory*", Westview Press, Reading, USA (1995).

[3] A. Wongel, "*Search for Heavy Resonances in Four-Top-Quark Final States in pp Collisions at $\sqrt{s}$ = 13 TeV With the ATLAS Detector*", Ph.D. thesis, Staats-und Universitätsbibliothek Hamburg Carl von Ossietzky, 2022.

[4] P.W. Higgs, "*Broken Symmetries and the Masses of Gauge Bosons*", *Phys. Rev. Lett.* **13** (1964) 508.

[5] F. Englert and R. Brout, "*Broken Symmetry and the Mass of Gauge Vector Mesons*", *Phys. Rev. Lett.* **13** (1964) 321.

[6] G.S. Guralnik, C.R. Hagen and T.W.B. Kibble, "*Global Conservation Laws and Massless Particles*", *Phys. Rev. Lett.* **13** (1964) 585.

[7] CMS collaboration, "*Observation of a New Boson at a Mass of 125 GeV with the CMS Experiment at the LHC*", *Phys. Lett. B* **716** (2012) 30 [1207.7235].

[8] ATLAS collaboration, "*Observation of a new particle in the search for the Standard Model Higgs boson with the ATLAS detector at the LHC*", *Phys. Lett. B* **716** (2012) 1 [1207.7214].

[9] A. Djouadi, "*The Anatomy of electro-weak symmetry breaking. I: The Higgs boson in the standard model*", *Phys. Rept.* **457** (2008) 1 [hep-ph/0503172].

[10] LHC Higgs Cross Section Working Group collaboration, "*Handbook of LHC Higgs Cross Sections: 4. Deciphering the Nature of the Higgs Sector*", 1610.07922.

[11] Particle Data Group collaboration, "*Review of Particle Physics*", *PTEP* **2022** (2022) 083C01.

[12] CMS collaboration, "*A portrait of the Higgs boson by the CMS experiment ten years after the discovery*", *Nature* **607** (2022) 60 [2207.00043].

[13] CMS collaboration, "*Observation of Higgs boson decay to bottom quarks*", *Phys. Rev. Lett.* **121** (2018) 121801 [1808.08242].

[14] CMS collaboration, "*Measurements of the Higgs boson production cross section and couplings in the W boson pair decay channel in proton-proton collisions at* $\sqrt{s} = 13\,TeV$", *Eur. Phys. J. C* **83** (2023) 667 [2206.09466].

[15] CMS collaboration, "*Observation of the Higgs boson decay to a pair of* τ *leptons with the CMS detector*", *Phys. Lett. B* **779** (2018) 283 [1708.00373].

[16] CMS collaboration, "*Search for Higgs Boson Decay to a Charm Quark-Antiquark Pair in Proton-Proton Collisions at s=13 TeV*", *Phys. Rev. Lett.* **131** (2023) 061801 [2205.05550].

[17] CMS collaboration, "*Measurements of Higgs boson production cross sections and couplings in the diphoton decay channel at* $\sqrt{\text{s}}$ *= 13 TeV*", *JHEP* **07** (2021) 027 [2103.06956].

[18] CMS collaboration, "*Search for Higgs boson decays to a Z boson and a photon in proton-proton collisions at* $\sqrt{s}$ *= 13 TeV*", *JHEP* **05** (2023) 233 [2204.12945].

[19] CMS collaboration, "*Evidence for Higgs boson decay to a pair of muons*", *JHEP* **01** (2021) 148 [2009.04363].

[20] G.-y. Huang and S. Zhou, "*Precise Values of Running Quark and Lepton Masses in the Standard Model*", *Phys. Rev. D* **103** (2021) 016010 [2009.04851].

[21] A.L. Kagan, G. Perez, F. Petriello et al., "*Exclusive Window onto Higgs Yukawa Couplings*", *Phys. Rev. Lett.* **114** (2015) 101802 [1406.1722].

[22] ATLAS collaboration, "*Searches for exclusive Higgs and Z boson decays into a vector quarkonium state and a photon using 139* fb^{-1} *of ATLAS* $\sqrt{s} = 13$ *TeV proton–proton collision data*", *Eur. Phys. J. C* **83** (2023) 781 [2208.03122].

[23] CMS collaboration, "*Search for rare decays of Z and Higgs bosons to* J/ψ *and a photon in proton-proton collisions at* $\sqrt{s} = 13$ *TeV*", *Eur. Phys. J. C* **79** (2019) 94 [1810.10056].

[24] ATLAS collaboration, "*Search for exclusive Higgs and Z boson decays to* $\phi\gamma$ *and* $\rho\gamma$ *with the ATLAS detector*", *JHEP* **07** (2018) 127 [1712.02758].

[25] ATLAS collaboration, "*Search for exclusive Higgs and Z boson decays to* $\omega\gamma$ *and Higgs boson decays to* $K^*\gamma$ *with the ATLAS detector*", 2301.09938.

[26] CMS collaboration, "*Search for Higgs boson decays into Z and J/ψ and for Higgs and Z boson decays into J/ψ or Y pairs in pp collisions at s=13 TeV*", *Phys. Lett. B* **842** (2023) 137534 [2206.03525].

[27] CMS collaboration, "*Search for decays of the 125 GeV Higgs boson into a Z boson and a* ρ *or* ϕ *meson*", *JHEP* **11** (2020) 039 [2007.05122].

[28] M. König and M. Neubert, "*Exclusive Radiative Higgs Decays as Probes of Light-Quark Yukawa Couplings*", *JHEP* **08** (2015) 012 [1505.03870].

[29] J.I. Aranda, G. González-Estrada, J. Montaño et al., "*Revisiting the rare* $H \to q_i q_j$ *decays in the standard model*", *J. Phys. G* **47** (2020) 125001 [2009.07166].

[30] FCC collaboration, "*FCC Physics Opportunities: Future Circular Collider Conceptual Design Report Volume 1*", *Eur. Phys. J. C* **79** (2019) 474.

[31] J. Ellis and T. You, "*Sensitivities of Prospective Future e+e- Colliders to Decoupled New Physics*", *JHEP* **03** (2016) 089 [1510.04561].

[32] D. d'Enterria, "*Physics case of FCC-ee*", *Frascati Phys. Ser.* **61** (2016) 17 [1601.06640].

[33] FCC collaboration, "*FCC-hh: The Hadron Collider: Future Circular Collider Conceptual Design Report Volume 3*", *Eur. Phys. J. ST* **228** (2019) 755.

[34] Gargamelle Neutrino collaboration, "*Observation of Neutrino Like Interactions Without Muon Or Electron in the Gargamelle Neutrino Experiment*", *Phys. Lett. B* **46** (1973) 138.

[35] UA1 collaboration, "*Experimental Observation of Isolated Large Transverse Energy Electrons with Associated Missing Energy at $\sqrt{s} = 540$ GeV*", *Phys. Lett. B* **122** (1983) 103.

[36] UA2 collaboration, "*Observation of Single Isolated Electrons of High Transverse Momentum in Events with Missing Transverse Energy at the CERN anti-p p Collider*", *Phys. Lett. B* **122** (1983) 476.

[37] ALEPH collaboration, "*Determination of the Number of Light Neutrino Species*", *Phys. Lett. B* **231** (1989) 519.

[38] NA48 collaboration, "*A New measurement of direct CP violation in two pion decays of the neutral kaon*", *Phys. Lett. B* **465** (1999) 335 [hep-ex/9909022].

[39] L. Evans and P. Bryant, "*LHC Machine*", *JINST* **3** (2008) S08001.

[40] CERN, "*Facts and figures about the LHC*", URL: https://home.cern/resources/faqs/facts-and-figures-about-lhc. Last accessed: October 10th 2023.

[41] E. Mobs, "*The CERN accelerator complex in 2019. Complexe des accélérateurs du CERN en 2019*", URL: https://cds.cern.ch/record/2684277, 2019. General Photo.

[42] ATLAS collaboration, "*ATLAS: Technical proposal for a general-purpose p p experiment at the Large Hadron Collider at CERN*", Geneva: CERN, 1994. - 272p. URL: https://cds.cern.ch/record/290968.

[43] CMS collaboration, "*CMS, the Compact Muon Solenoid: Technical proposal*", Geneva: CERN, 1994. - 254p. URL: https://cds.cern.ch/record/290969.

[44] ALICE collaboration, "*ALICE: Technical proposal for a large ion collider experiment at the CERN LHC*", Geneva: CERN, 1995. - 237p. URL: https://cds.cern.ch/record/293391.

[45] LHCb collaboration, "*LHCb technical proposal: A Large Hadron Collider Beauty Experiment for Precision Measurements of CP Violation and Rare Decays*", Geneva: CERN, 1998. - 170p. URL: https://cds.cern.ch/record/622031.

[46] CMS collaboration, "*CMS Luminosity - Public Results*", URL: https://twiki.cern.ch/twiki/bin/view/CMSPublic/LumiPublicResults, 2023. Last accessed: October 10th 2023.

[47] CMS collaboration, "*The CMS Experiment at the CERN LHC*", *JINST* **3** (2008) S08004.

[48] CMS collaboration, G.L. Bayatian et al., "*CMS Physics: Technical Design Report Volume 1: Detector Performance and Software*", Technical design report. CMS, CERN, Geneva (2006).

[49] T. Sakuma and T. McCauley, "*Detector and Event Visualization with SketchUp at the CMS Experiment*", *J. Phys. Conf. Ser.* **513** (2014) 022032 [1311.4942].

[50] D. Barney, "*CMS Detector Slice*", 2016. CMS Collection. URL: https://cds.cern.ch/record/2120661.

[51] A. Buckley, C. White and M. White, "*Practical Collider Physics*", IOP (12, 2021), 10.1088/978-0-7503-2444-1.

[52] CERN, "*The CERN Experimental Programme - CMS*", URL: https://greybook.cern.ch/experiment/detail?id=CMS. Last accessed: October 11th 2023.

[53] ALEPH, CDF, D0, DELPHI, L3, OPAL, SLD, LEP Electroweak Working Group, Tevatron Electroweak Working Group, SLD Electroweak, Heavy Flavour Groups collaboration, "*Precision Electroweak Measurements and Constraints on the Standard Model*", 1012.2367.

[54] LEP Working Group for Higgs boson searches, ALEPH, DELPHI, L3, OPAL collaboration, "*Search for the standard model Higgs boson at LEP*", *Phys. Lett. B* **565** (2003) 61 [hep-ex/0306033].

[55] CMS collaboration, "*The CMS NanoAOD data tier*", URL: https://twiki.cern.ch/twiki/bin/view/CMSPublic/WorkBookNanoAOD, 2023. Last accessed: October 16th 2023.

[56] CMS collaboration, "*ROOT: Data Analysis Framework*", URL: https://root.cern/, 2023. Last accessed: October 16th 2023.

[57] J. Alwall, R. Frederix, S. Frixione et al., "*The automated computation of tree-level and next-to-leading order differential cross sections, and their matching to parton shower simulations*", *JHEP* **07** (2014) 079 [1405.0301].

[58] S. Alioli, P. Nason, C. Oleari et al., "*A general framework for implementing NLO calculations in shower Monte Carlo programs: the POWHEG BOX*", *JHEP* **06** (2010) 043 [1002.2581].

[59] T. Sjöstrand, S. Ask, J.R. Christiansen et al., "*An introduction to PYTHIA 8.2*", *Comput. Phys. Commun.* **191** (2015) 159 [1410.3012].

[60] NNPDF collaboration, "*Parton distributions from high-precision collider data*", *Eur. Phys. J. C* **77** (2017) 663 [1706.00428].

[61] CMS collaboration, "*Extraction and validation of a new set of CMS PYTHIA8 tunes from underlying-event measurements*", *Eur. Phys. J. C* **80** (2020) 4 [1903.12179].

[62] CMS collaboration, "*CMS track reconstruction performance during Run 2 and developments for Run 3*", *PoS* **ICHEP2020** (2021) 733 [2012.07035].

[63] CERN collaboration, "*Cross Section DB Tool (XSecDB)*", URL: https://xsdb-temp.app.cern.ch/, 2023. Last accessed: October 16th 2023.

[64] CMS collaboration, "*Measurement of differential cross sections for inclusive isolated-photon and photon+jets production in proton-proton collisions at $\sqrt{s} = 13$ TeV*", *Eur. Phys. J. C* **79** (2019) 20 [1807.00782].

[65] K. Hamilton, P. Nason and G. Zanderighi, "*MINLO: Multi-Scale Improved NLO*", *JHEP* **10** (2012) 155 [1206.3572].

[66] D. Contardo, M. Klute, J. Mans et al., "*Technical Proposal for the Phase-II Upgrade of the CMS Detector*", CERN, Geneva (2015), DOI.

[67] M. Cacciari, G.P. Salam and G. Soyez, "*FastJet User Manual*", *Eur. Phys. J. C* **72** (2012) 1896 [1111.6097].

[68] CMS collaboration, "*Study of Pileup Removal Algorithms for Jets*", CERN, Geneva (2014).

[69] CMS collaboration, "*Pileup measurement and mitigation techniques in CMS*", *J. Phys. Conf. Ser.* **404** (2012) 012045.

[70] E. Bols, J. Kieseler, M. Verzetti et al., "*Jet Flavour Classification Using DeepJet*", *JINST* **15** (2020) P12012 [2008.10519].

[71] Y. Feng, "*A New Deep-Neural-Network–Based Missing Transverse Momentum Estimator, and its Application to W Recoil*", Ph.D. thesis, Maryland U., 2020.

[72] CMS collaboration, "*Electron and photon reconstruction and identification with the CMS experiment at the CERN LHC*", *JINST* **16** (2021) P05014 [2012.06888].

[73] CMS collaboration, "*CMS Electron and Photon Performance at 13 TeV*", *J. Phys. Conf. Ser.* **1162** (2019) 012008.

[74] CMS collaboration, "*Description and performance of track and primary-vertex reconstruction with the CMS tracker*", *JINST* **9** (2014) P10009 [1405.6569].

[75] CMS collaboration, "*CMSSW on GitHub*", URL: https://cms-sw.github.io/, 2023. Last accessed: October 18th 2023.

[76] K. Prokofiev and T. Speer, "*A kinematic and a decay chain reconstruction library*", in *14th International Conference on Computing in High-Energy and Nuclear Physics*, pp. 411–414, 2005, DOI.

[77] TMVA collaboration, "*TMVA - Toolkit for Multivariate Data Analysis*", physics/0703039.

[78] Y. Coadou, "*Boosted decision trees*", 2206.09645.